

AD-A254 525



Submitted

February 10, 1992

to *Journal of The Acoustical Society of America*

Near-normal incidence scattering from rough, finite surfaces:

Kirchhoff theory and data comparison for arctic sea ice

P. D. Mourad and K. L. Williams

DTIC
ELECTED
AUG 3 1992
S C D

*Applied Physics Laboratory, College of Ocean and Fishery Sciences,
University of Washington, 1013 N.E. 40th Street, Seattle, WA. 98105-6698*

Received:



031700
92-20935⁵⁷



92 8 9 10 20935

ABSTRACT

We apply Kirchhoff theory for the target strength of a rough, circular surface whose roughness is characterized by a two-dimensional, isotropic power-law wavenumber spectrum, $W_2(\kappa) = \eta_2 \kappa^{-p_2}$. Three nondimensional parameters are found that govern the target strength: $\zeta = \kappa_0 a$, $\eta = \eta_2 a^{p_2 - 4}$, and $p_1 = p_2 - 1$, where κ_0 is the acoustic wavenumber, a is the radius of the surface, and p_1 is the spectral exponent of the one-dimensional power-law wavenumber spectrum. First, we discuss the general influence of ζ , p_1 , and η on the target strength. Following that are calculations of average target strength of the ice/water interface of a submerged cylindrical block of ice, which are compared with individual realizations of measured target strengths of ice blocks for frequencies between 20 kHz and 80 kHz. Data and theory show that the (smooth surface) form function for a finite surface does not describe the observed diffraction pattern. Instead, the lobes of the pattern diminish and the nulls fill in — i.e., the total backscatter becomes more incoherent — as frequency increases or as the large wavenumber components of the roughness spectrum contribute more to the total acoustic return. These comparisons also allowed us to infer the rough surface statistics of the ice surface and the compressional sound speed structure within the skeletal zone of the ice.

PACS numbers 43.20.F, 43.20.R, 43.30.G, 43.30.H, 43.30.M

43.20.F, 43.30.H, 43.30.Pc

Statement A per telecon Thomas Curtin
ONR/Code 1125
Arlington, VA 22217-5000

NWW 8/5/92

Acceleration For	<input checked="" type="checkbox"/>
Navigation	<input type="checkbox"/>
Orbit Plan	<input type="checkbox"/>
Orbital Period	<input type="checkbox"/>
Orbital Eccentricity	<input type="checkbox"/>
Orbital Inclination	<input type="checkbox"/>
Orbital Perigee	<input type="checkbox"/>
Orbital Apogee	<input type="checkbox"/>
Orbital Period	<input type="checkbox"/>
Orbital Eccentricity	<input type="checkbox"/>
Orbital Inclination	<input type="checkbox"/>
Orbital Perigee	<input type="checkbox"/>
Orbital Apogee	<input type="checkbox"/>
Orbital Period	<input type="checkbox"/>
Orbital Eccentricity	<input type="checkbox"/>
Orbital Inclination	<input type="checkbox"/>
Orbital Perigee	<input type="checkbox"/>
Orbital Apogee	<input type="checkbox"/>
Orbital Period	<input type="checkbox"/>
Orbital Eccentricity	<input type="checkbox"/>
Orbital Inclination	<input type="checkbox"/>
Orbital Perigee	<input type="checkbox"/>
Orbital Apogee	<input type="checkbox"/>
Orbital Period	<input type="checkbox"/>
Orbital Eccentricity	<input type="checkbox"/>
Orbital Inclination	<input type="checkbox"/>
Orbital Perigee	<input type="checkbox"/>
Orbital Apogee	<input type="checkbox"/>
Orbital Period	<input type="checkbox"/>
Orbital Eccentricity	<input type="checkbox"/>
Orbital Inclination	<input type="checkbox"/>
Orbital Perigee	<input type="checkbox"/>
Orbital Apogee	<input type="checkbox"/>
Orbital Period	<input type="checkbox"/>
Orbital Eccentricity	<input type="checkbox"/>
Orbital Inclination	<input type="checkbox"/>
Orbital Perigee	<input type="checkbox"/>
Orbital Apogee	<input type="checkbox"/>
Orbital Period	<input type="checkbox"/>
Orbital Eccentricity	<input type="checkbox"/>
Orbital Inclination	<input type="checkbox"/>
Orbital Perigee	<input type="checkbox"/>
Orbital Apogee	<input type="checkbox"/>
Orbital Period	<input type="checkbox"/>
Orbital Eccentricity	<input type="checkbox"/>
Orbital Inclination	<input type="checkbox"/>
Orbital Perigee	<input type="checkbox"/>
Orbital Apogee	<input type="checkbox"/>
Orbital Period	<input type="checkbox"/>
Orbital Eccentricity	<input type="checkbox"/>
Orbital Inclination	<input type="checkbox"/>
Orbital Perigee	<input type="checkbox"/>
Orbital Apogee	<input type="checkbox"/>
Orbital Period	<input type="checkbox"/>
Orbital Eccentricity	<input type="checkbox"/>
Orbital Inclination	<input type="checkbox"/>
Orbital Perigee	<input type="checkbox"/>
Orbital Apogee	<input type="checkbox"/>
Orbital Period	<input type="checkbox"/>
Orbital Eccentricity	<input type="checkbox"/>
Orbital Inclination	<input type="checkbox"/>
Orbital Perigee	<input type="checkbox"/>
Orbital Apogee	<input type="checkbox"/>
Orbital Period	<input type="checkbox"/>
Orbital Eccentricity	<input type="checkbox"/>
Orbital Inclination	<input type="checkbox"/>
Orbital Perigee	<input type="checkbox"/>
Orbital Apogee	<input type="checkbox"/>
Orbital Period	<input type="checkbox"/>
Orbital Eccentricity	<input type="checkbox"/>
Orbital Inclination	<input type="checkbox"/>
Orbital Perigee	<input type="checkbox"/>
Orbital Apogee	<input type="checkbox"/>
Orbital Period	<input type="checkbox"/>
Orbital Eccentricity	<input type="checkbox"/>
Orbital Inclination	<input type="checkbox"/>
Orbital Perigee	<input type="checkbox"/>
Orbital Apogee	<input type="checkbox"/>
Orbital Period	<input type="checkbox"/>
Orbital Eccentricity	<input type="checkbox"/>
Orbital Inclination	<input type="checkbox"/>
Orbital Perigee	<input type="checkbox"/>
Orbital Apogee	<input type="checkbox"/>
Orbital Period	<input type="checkbox"/>
Orbital Eccentricity	<input type="checkbox"/>
Orbital Inclination	<input type="checkbox"/>
Orbital Perigee	<input type="checkbox"/>
Orbital Apogee	<input type="checkbox"/>
Orbital Period	<input type="checkbox"/>
Orbital Eccentricity	<input type="checkbox"/>
Orbital Inclination	<input type="checkbox"/>
Orbital Perigee	<input type="checkbox"/>
Orbital Apogee	<input type="checkbox"/>
Orbital Period	<input type="checkbox"/>
Orbital Eccentricity	<input type="checkbox"/>
Orbital Inclination	<input type="checkbox"/>
Orbital Perigee	<input type="checkbox"/>
Orbital Apogee	<input type="checkbox"/>
Orbital Period	<input type="checkbox"/>
Orbital Eccentricity	<input type="checkbox"/>
Orbital Inclination	<input type="checkbox"/>
Orbital Perigee	<input type="checkbox"/>
Orbital Apogee	<input type="checkbox"/>
Orbital Period	<input type="checkbox"/>
Orbital Eccentricity	<input type="checkbox"/>
Orbital Inclination	<input type="checkbox"/>
Orbital Perigee	<input type="checkbox"/>
Orbital Apogee	<input type="checkbox"/>
Orbital Period	<input type="checkbox"/>
Orbital Eccentricity	<input type="checkbox"/>
Orbital Inclination	<input type="checkbox"/>
Orbital Perigee	<input type="checkbox"/>
Orbital Apogee	<input type="checkbox"/>
Orbital Period	<input type="checkbox"/>
Orbital Eccentricity	<input type="checkbox"/>
Orbital Inclination	<input type="checkbox"/>
Orbital Perigee	<input type="checkbox"/>
Orbital Apogee	<input type="checkbox"/>
Orbital Period	<input type="checkbox"/>
Orbital Eccentricity	<input type="checkbox"/>
Orbital Inclination	<input type="checkbox"/>
Orbital Perigee	<input type="checkbox"/>
Orbital Apogee	<input type="checkbox"/>
Orbital Period	<input type="checkbox"/>
Orbital Eccentricity	<input type="checkbox"/>
Orbital Inclination	<input type="checkbox"/>
Orbital Perigee	<input type="checkbox"/>
Orbital Apogee	<input type="checkbox"/>
Orbital Period	<input type="checkbox"/>
Orbital Eccentricity	<input type="checkbox"/>
Orbital Inclination	<input type="checkbox"/>
Orbital Perigee	<input type="checkbox"/>
Orbital Apogee	<input type="checkbox"/>
Orbital Period	<input type="checkbox"/>
Orbital Eccentricity	<input type="checkbox"/>
Orbital Inclination	<input type="checkbox"/>
Orbital Perigee	<input type="checkbox"/>
Orbital Apogee	<input type="checkbox"/>
Orbital Period	<input type="checkbox"/>
Orbital Eccentricity	<input type="checkbox"/>
Orbital Inclination	<input type="checkbox"/>
Orbital Perigee	<input type="checkbox"/>
Orbital Apogee	<input type="checkbox"/>
Orbital Period	<input type="checkbox"/>
Orbital Eccentricity	<input type="checkbox"/>
Orbital Inclination	<input type="checkbox"/>
Orbital Perigee	<input type="checkbox"/>
Orbital Apogee	<input type="checkbox"/>
Orbital Period	<input type="checkbox"/>
Orbital Eccentricity	<input type="checkbox"/>
Orbital Inclination	<input type="checkbox"/>
Orbital Perigee	<input type="checkbox"/>
Orbital Apogee	<input type="checkbox"/>
Orbital Period	<input type="checkbox"/>
Orbital Eccentricity	<input type="checkbox"/>
Orbital Inclination	<input type="checkbox"/>
Orbital Perigee	<input type="checkbox"/>
Orbital Apogee	<input type="checkbox"/>
Orbital Period	<input type="checkbox"/>
Orbital Eccentricity	<input type="checkbox"/>
Orbital Inclination	<input type="checkbox"/>
Orbital Perigee	<input type="checkbox"/>
Orbital Apogee	<input type="checkbox"/>
Orbital Period	<input type="checkbox"/>
Orbital Eccentricity	<input type="checkbox"/>
Orbital Inclination	<input type="checkbox"/>
Orbital Perigee	<input type="checkbox"/>
Orbital Apogee	<input type="checkbox"/>
Orbital Period	<input type="checkbox"/>
Orbital Eccentricity	<input type="checkbox"/>
Orbital Inclination	<input type="checkbox"/>
Orbital Perigee	<input type="checkbox"/>
Orbital Apogee	<input type="checkbox"/>
Orbital Period	<input type="checkbox"/>
Orbital Eccentricity	<input type="checkbox"/>
Orbital Inclination	<input type="checkbox"/>
Orbital Perigee	<input type="checkbox"/>
Orbital Apogee	<input type="checkbox"/>
Orbital Period	<input type="checkbox"/>
Orbital Eccentricity	<input type="checkbox"/>
Orbital Inclination	<input type="checkbox"/>
Orbital Perigee	<input type="checkbox"/>
Orbital Apogee	<input type="checkbox"/>
Orbital Period	<input type="checkbox"/>
Orbital Eccentricity	<input type="checkbox"/>
Orbital Inclination	<input type="checkbox"/>
Orbital Perigee	<input type="checkbox"/>
Orbital Apogee	<input type="checkbox"/>
Orbital Period	<input type="checkbox"/>
Orbital Eccentricity	<input type="checkbox"/>
Orbital Inclination	<input type="checkbox"/>
Orbital Perigee	<input type="checkbox"/>
Orbital Apogee	<input type="checkbox"/>
Orbital Period	<input type="checkbox"/>
Orbital Eccentricity	<input type="checkbox"/>
Orbital Inclination	<input type="checkbox"/>
Orbital Perigee	<input type="checkbox"/>
Orbital Apogee	<input type="checkbox"/>
Orbital Period	<input type="checkbox"/>
Orbital Eccentricity	<input type="checkbox"/>
Orbital Inclination	<input type="checkbox"/>
Orbital Perigee	<input type="checkbox"/>
Orbital Apogee	<input type="checkbox"/>
Orbital Period	<input type="checkbox"/>
Orbital Eccentricity	<input type="checkbox"/>
Orbital Inclination	<input type="checkbox"/>
Orbital Perigee	<input type="checkbox"/>
Orbital Apogee	<input type="checkbox"/>
Orbital Period	<input type="checkbox"/>
Orbital Eccentricity	<input type="checkbox"/>
Orbital Inclination	<input type="checkbox"/>
Orbital Perigee	<input type="checkbox"/>
Orbital Apogee	<input type="checkbox"/>
Orbital Period	<input type="checkbox"/>
Orbital Eccentricity	<input type="checkbox"/>
Orbital Inclination	<input type="checkbox"/>
Orbital Perigee	<input type="checkbox"/>
Orbital Apogee	<input type="checkbox"/>
Orbital Period	<input type="checkbox"/>
Orbital Eccentricity	<input type="checkbox"/>
Orbital Inclination	<input type="checkbox"/>
Orbital Perigee	<input type="checkbox"/>
Orbital Apogee	<input type="checkbox"/>
Orbital Period	<input type="checkbox"/>
Orbital Eccentricity	<input type="checkbox"/>
Orbital Inclination	<input type="checkbox"/>
Orbital Perigee	<input type="checkbox"/>
Orbital Apogee	<input type="checkbox"/>
Orbital Period	<input type="checkbox"/>
Orbital Eccentricity	<input type="checkbox"/>
Orbital Inclination	<input type="checkbox"/>
Orbital Perigee	<input type="checkbox"/>
Orbital Apogee	<input type="checkbox"/>
Orbital Period	<input type="checkbox"/>
Orbital Eccentricity	<input type="checkbox"/>
Orbital Inclination	<input type="checkbox"/>
Orbital Perigee	<input type="checkbox"/>
Orbital Apogee	<input type="checkbox"/>
Orbital Period	<input type="checkbox"/>
Orbital Eccentricity	<input type="checkbox"/>
Orbital Inclination	<input type="checkbox"/>
Orbital Perigee	<input type="checkbox"/>
Orbital Apogee	<input type="checkbox"/>
Orbital Period	<input type="checkbox"/>
Orbital Eccentricity	<input type="checkbox"/>
Orbital Inclination	<input type="checkbox"/>
Orbital Perigee	<input type="checkbox"/>
Orbital Apogee	<input type="checkbox"/>
Orbital Period	<input type="checkbox"/>
Orbital Eccentricity	<input type="checkbox"/>
Orbital Inclination	<input type="checkbox"/>
Orbital Perigee	<input type="checkbox"/>
Orbital Apogee	<input type="checkbox"/>
Orbital Period	<input type="checkbox"/>
Orbital Eccentricity	<input type="checkbox"/>
Orbital Inclination	<input type="checkbox"/>
Orbital Perigee	<input type="checkbox"/>
Orbital Apogee	<input type="checkbox"/>
Orbital Period	<input type="checkbox"/>
Orbital Eccentricity	<input type="checkbox"/>
Orbital Inclination	<input type="checkbox"/>
Orbital Perigee	<input type="checkbox"/>
Orbital Apogee	<input type="checkbox"/>
Orbital Period	<input type="checkbox"/>
Orbital Eccentricity	<input type="checkbox"/>
Orbital Inclination	<input type="checkbox"/>
Orbital Perigee	<input type="checkbox"/>
Orbital Apogee	<input type="checkbox"/>
Orbital Period	<input type="checkbox"/>
Orbital Eccentricity	<input type="checkbox"/>
Orbital Inclination	<input type="checkbox"/>
Orbital Perigee	<input type="checkbox"/>
Orbital Apogee	<input type="checkbox"/>
Orbital Period	<input type="checkbox"/>
Orbital Eccentricity	<input type="checkbox"/>
Orbital Inclination	<input type="checkbox"/>
Orbital Perigee	<input type="checkbox"/>
Orbital Apogee	<input type="checkbox"/>
Orbital Period	<input type="checkbox"/>
Orbital Eccentricity	<input type="checkbox"/>
Orbital Inclination	<input type="checkbox"/>
Orbital Perigee	<input type="checkbox"/>
Orbital Apogee	<input type="checkbox"/>
Orbital Period	<input type="checkbox"/>
Orbital Eccentricity	<input type="checkbox"/>
Orbital Inclination	<input type="checkbox"/>
Orbital Perigee	<input type="checkbox"/>
Orbital Apogee	<input type="checkbox"/>
Orbital Period	<input type="checkbox"/>
Orbital Eccentricity	<input type="checkbox"/>
Orbital Inclination	<input type="checkbox"/>
Orbital Perigee	<input type="checkbox"/>
Orbital Apogee	<input type="checkbox"/>
Orbital Period	<input type="checkbox"/>
Orbital Eccentricity	<input type="checkbox"/>
Orbital Inclination	<input type="checkbox"/>
Orbital Perigee	<input type="checkbox"/>
Orbital Apogee	<input type="checkbox"/>
Orbital Period	<input type="checkbox"/>
Orbital Eccentricity	<input type="checkbox"/>
Orbital Inclination	<input type="checkbox"/>
Orbital Perigee	<input type="checkbox"/>
Orbital Apogee	<input type="checkbox"/>
Orbital Period	<input type="checkbox"/>
Orbital Eccentricity	<input type="checkbox"/>
Orbital Inclination	<input type="checkbox"/>
Orbital Perigee	<input type="checkbox"/>
Orbital Apogee	<input type="checkbox"/>
Orbital Period	<input type="checkbox"/>
Orbital Eccentricity	<input type="checkbox"/>
Orbital Inclination	<input type="checkbox"/>
Orbital Perigee	<input type="checkbox"/>
Orbital Apogee	<input type="checkbox"/>
Orbital Period	<input type="checkbox"/>
Orbital Eccentricity	<input type="checkbox"/>
Orbital Inclination	<input type="checkbox"/>
Orbital Perigee	<input type="checkbox"/>
Orbital Apogee	<input type="checkbox"/>
Orbital Period	<input type="checkbox"/>
Orbital Eccentricity	<input type="checkbox"/>
Orbital Inclination	<input type="checkbox"/>
Orbital Perigee	<input type="checkbox"/>
Orbital Apogee	<input type="checkbox"/>
Orbital Period	<input type="checkbox"/>
Orbital Eccentricity	<input type="checkbox"/>
Orbital Inclination	<input type="checkbox"/>
Orbital Perigee	<input type="checkbox"/>
Orbital Apogee	<input type="checkbox"/>
Orbital Period	<input type="checkbox"/>
Orbital Eccentricity	<input type="checkbox"/>
Orbital Inclination	<input type="checkbox"/>
Orbital Perigee	<input type="checkbox"/>
Orbital Apogee	<input type="checkbox"/>
Orbital Period	<input type="checkbox"/>
Orbital Eccentricity	<input type="checkbox"/>
Orbital Inclination	<input type="checkbox"/>
Orbital Perigee	<input type="checkbox"/>
Orbital Apogee	<input type="checkbox"/>
Orbital Period	<input type="checkbox"/>
Orbital Eccentricity	<input type="checkbox"/>
Orbital Inclination	<input type="checkbox"/>
Orbital Perigee	<input type="checkbox"/>
Orbital Apogee	<input type="checkbox"/>
Orbital Period	<input type="checkbox"/>
Orbital Eccentricity	<input type="checkbox"/>
Orbital Inclination	<input type="checkbox"/>
Orbital Perigee	<input type="checkbox"/>
Orbital Apogee	<input type="checkbox"/>
Orbital Period	<input type="checkbox"/>
Orbital Eccentricity	<input type="checkbox"/>
Orbital Inclination	<input type="checkbox"/>
Orbital Perigee	<input type="checkbox"/>
Orbital Apogee	<input type="checkbox"/>
Orbital Period	<input type="checkbox"/>
Orbital Eccentricity	<input type="checkbox"/>
Orbital Inclination	<input type="checkbox"/>
Orbital Perigee	<input type="checkbox"/>
Orbital Apogee	<input type="checkbox"/>
Orbital Period	<input type="checkbox"/>
Orbital Eccentricity	<input type="checkbox"/>
Orbital Inclination	<input type="checkbox"/>
Orbital Perigee	<input type="checkbox"/>
Orbital Apogee	<input type="checkbox"/>
Orbital Period	<input type="checkbox"/>
Orbital Eccentricity	<input type="checkbox"/>
Orbital Inclination	<input type="checkbox"/>
Orbital Perigee	<input type="checkbox"/>
Orbital Apogee	<input type="checkbox"/>
Orbital Period	<input type="checkbox"/>
Orbital Eccentricity	<input type="checkbox"/>
Orbital Inclination	<input type="checkbox"/>
Orbital Perigee	<input type="checkbox"/>
Orbital Apogee	<input type="checkbox"/>
Orbital Period	<input type="checkbox"/>
Orbital Eccentricity	<input type="checkbox"/>
Orbital Inclination	<input type="checkbox"/>
Orbital Perigee	<input type="checkbox"/>
Orbital Apogee	<input type="checkbox"/>
Orbital Period	<input type="checkbox"/>
Orbital Eccentricity	<input type="checkbox"/>
Orbital Inclination	<input type="checkbox"/>
Orbital Perigee	<input type="checkbox"/>
Orbital Apogee	<input type="checkbox"/>
Orbital Period	<input type="checkbox"/>
Orbital Eccentricity	<input type="checkbox"/>
Orbital Inclination	<input type="checkbox"/>
Orbital Perigee	<input type="checkbox"/>
Orbital Apogee	<input type="checkbox"/>
Orbital Period	<input type="checkbox"/>
Orbital Eccentricity	<input type="checkbox"/>
Orbital Inclination	<input type="checkbox"/>
Orbital Perigee	<input type="checkbox"/>
Orbital Apogee	<input type="checkbox"/>
Orbital Period	<input type="checkbox"/>
Orbital Eccentricity	<input type="checkbox"/>
Orbital Inclination	<input type="checkbox"/>
Orbital Perigee	<input type="checkbox"/>
Orbital Apogee	<input type="checkbox"/>
Orbital Period	<input type="checkbox"/>
Orbital Eccentricity	<input type="checkbox"/>
Orbital Inclination	<input type="checkbox"/>
Orbital Perigee	<input type="checkbox"/>
Orbital Apogee	<input type="checkbox"/>
Orbital Period	<input type="checkbox"/>
Orbital Eccentricity	<input type="checkbox"/>
Orbital Inclination	<input type="checkbox"/>
Orbital Perigee	<input type="checkbox"/>
Orbital Apogee	<input type="checkbox"/>
Orbital Period	<input type="checkbox"/>
Orbital Eccentricity	<input type="checkbox"/>
Orbital Inclination	<input type="checkbox"/>
Orbital Perigee	<input type="checkbox"/>
Orbital Apogee	<input type="checkbox"/>
Orbital Period	<input type="checkbox"/>
Orbital Eccentricity	<input type="checkbox"/>
Orbital Inclination	<input type="checkbox"/>
Orbital Perigee	<input type="checkbox"/>
Orbital Apogee	<input type="checkbox"/>
Orbital Period	<input type="checkbox"/>
Orbital Eccentricity	<input type="checkbox"/>
Orbital Inclination	<input type="checkbox"/>
Orbital Perigee	<input type="checkbox"/>
Orbital Apogee	<input type="checkbox"/>
Orbital Period	<input type="checkbox"/>
Orbital Eccentricity	<input type="checkbox"/>
Orbital Inclination	<input type="checkbox"/>
Orbital Perigee	<input type="checkbox"/>
Orbital Apogee	

INTRODUCTION

The goals of our research are twofold: to develop a theory for total backscatter from rough, finite surfaces near normal incidence, and to use this theory to understand the scattering of sound from undeformed, first-year arctic sea ice. Our analysis, based on Kirchhoff theory, breaks down the backscatter into the product of two parts. One is a "rough surface form function," which captures the effects on the backscatter due to the rough, finite interface. The other is the reflection coefficient of the surface, which captures the material's intrinsic properties, such as its density and compressive sound speed structure.

This work is of interest because existing models for high-frequency backscatter from first-year arctic ice keels (Bishop et al., 1987) assume the keels are made up of a collection of uncorrelated, rectangular ice blocks that are *smooth*, and whose individual faces reflect energy back to the acoustic source. In nature, there are many examples of rough, finite interfaces; thus study of the factors that determine the acoustic return from a finite, rough object is also of general interest.

In this article, we review data that support the use of a rough-surface scattering mechanism for individual blocks. We then develop a theory, based on the Kirchhoff approximation, that addresses these observations.

REVIEW OF EXPERIMENTS

Our study was motivated by observations of acoustic reflection from the bottom of arctic ice blocks by Garrison et al. (1991). Figure 1 shows their generic experimental setup. A cylindrical "block" was cored out of the ice sheet; a typical length was 1 m and the diameter about 0.5 m. This block was submerged below the ice canopy, where it was ensonified by a transducer suspended at the vertex of a triad of cables. The cables were manipulated so that sound struck the block over a range of angles near normal incidence. Acoustic returns from the ice block were calibrated by ensonifying a submerged, flat, air-filled pan which had the same horizontal dimensions as the ice block and had been lowered to the same depth as the lower face of the block.

These experiments resulted in measurements of the calibrated target strength of the ice/water interface of several ice blocks near normal incidence. Their data were for the acoustic return from the ice-bottom/water interface only; all other contributions to the acoustic backscatter were time-gated out.

Figure 2 contains representative samples of the resulting data. The column on the left shows the acoustic return from the air-filled pan compared with what is essentially the Fraunhoffer diffraction pattern for a rigid, circular plate. There are minor, near-field corrections (a reduction in the strict Fraunhoffer beam pattern of less than 1 to 2 dB), but these are relevant only at 80 kHz.

FIG. 1

FIG. 2

The strong correlation between theory and experiment for the deterministic surface represented by the air-filled pan (restricted to between $\pm 5^\circ$ for 80 kHz) shows the efficacy of the experimental method. It also shows that the source and scatterers were far enough apart that the Fraunhofer assumption holds.

The right-hand column of Fig. 2 shows individual realizations of the acoustic return from a submerged ice block at several frequencies compared with the Fraunhofer diffraction pattern used in the air-pan observation. There were not enough realizations to define average target strengths, but these are representative of the few individual realizations displayed by Garrison et al. (1991). Compared with the smooth-faced acoustic return, the ice-block data show a reduction in the target strength of the return at normal incidence, as well as a smoothing of the rigid-plate side-lobe structure. Both of these trends become more pronounced as the acoustic frequency increases.

We explain these frequency-dependent variations in target strength, arguing that both the rough surface of the ice and the sound speed variations within the ice contribute to the target strength of a finite ice block.

THEORY

Consider the Kirchhoff approximation in the Fraunhofer limit for the sound scattered from a rough, finite shape ensonified by a point source. Tolstoy and Clay (1966) developed this formula for an infinite surface and included a point-source beam pattern.

We use their formula, but for a finite surface and omnidirectional sources.

Figure 3 shows the rectangular coordinate system. The angle between the incident wave and the z-axis of the coordinate system is labeled θ_1 , and that between the scattered components and the z-axis is θ_0 . The acoustic wavenumber is $\kappa_0 = \omega/c$, where $c = 1437$ m/s for arctic conditions. The total scattered pressure is given by

$$P(r_0) = \frac{iB}{2\pi |\vec{r}_0| |\vec{r}_1|} e^{i\kappa_0(|\vec{r}_0| + |\vec{r}_1|)} \quad (1)$$

$$\times \int_A \int \kappa_0 R(\alpha h_x + \beta h_y - \gamma) e^{2\kappa_0 i [\alpha x + \beta y + h(x, y)]} dx dy ;$$

$$2\alpha \equiv (\sin\theta_1 \cos\psi_1 - \sin\theta_0 \cos\psi_0), \quad (2)$$

$$2\beta \equiv (\sin\theta_1 \sin\psi_1 - \sin\theta_0 \sin\psi_0), \quad (3)$$

$$2\gamma \equiv -(\cos\theta_1 + \cos\theta_0). \quad (4)$$

The function $h(x, y)$ defines the two-dimensional scattering surface. For back-scatter, $\psi_0 = 0$, $\psi_1 = \pi$, and $\theta_0 = \theta_1$. The constant B is the source level and R is the reflection coefficient of the surface, based on the intrinsic impedance mismatch between the ice and the water. We have modeled the ice as a fluid with equivalent compressional sound speed and density. At normal incidence, only compressional waves enter the ice from the water. We assume that the contributions to Green's theorem from the contours along the sides of the block are negligible for the narrow range of angles considered.

Fig
3

At this point, the standard procedure is to integrate by parts, generating an integral with a more compact integrand and two boundary terms. For example, consider the following subintegral in Eq. (1) (with explicit boundary conditions chosen for didactic purposes):

$$\begin{aligned}
 \int_a^b \alpha h_x e^{2i\kappa_0[\alpha x + \gamma h(x,y)]} dx &= \int_a^b \alpha e^{2i\kappa_0 \alpha x} [h_x e^{2i\kappa_0 \gamma h(x,y)}] dx \\
 &= \frac{\alpha}{2i\kappa_0 \gamma} e^{2i\kappa_0[\alpha x + \gamma h(x,y)]} \Big|_{x=a}^{x=b} \\
 &\quad - \int_a^b \frac{\alpha^2}{\gamma} e^{2i\kappa_0[\alpha x + \gamma h(x,y)]} dx. \tag{5}
 \end{aligned}$$

Similar expressions can be obtained for the other two subintegrals. The boundary terms are usually discarded for infinite surfaces by including a bounded beam whose surface field goes to zero at large distances from the source. For a finite surface, the boundary terms remain. In Appendix A we examine their contribution for a one-dimensional (rather than two-dimensional) surface. We find that these boundary terms do not significantly contribute to the total backscattered intensity for the parameter values relevant to our problem.

Substitution of the remaining integral relations into Eq. (1) produces the standard expression for the total backscattered pressure, P :

$$P = \frac{-iB}{2\pi |\vec{r}_0| |\vec{r}_1|} e^{i\kappa_0(|\vec{r}_0| + |\vec{r}_1|)}$$

$$\times \frac{\kappa_0 R}{\gamma} (\alpha^2 + \beta^2 + \gamma^2) \int_A \int e^{2i\kappa_0 [\alpha x + \beta y + \gamma h(x,y)]} dx dy . \quad (6)$$

The quantities α , β , and γ and the reflection coefficient R are functions of the incident grazing angle θ_i . We restrict our attention to angles close to normal incidence and will consider these angular functions to be constant. We can then re-write (6) as follows:

$$P = Q \left(\frac{\pi}{2} \right) \Theta , \quad (7)$$

$$Q(\theta_i) = \frac{-iBf(\theta_i)\kappa_0 R}{2\pi |\vec{r}_0| |\vec{r}_1|} e^{i\kappa_0 (|\vec{r}_0| + |\vec{r}_1|)} , \quad (8)$$

where

$$f(\theta_i) \equiv \frac{1}{\gamma} (\alpha^2 + \beta^2 + \gamma^2) , \quad (9)$$

and

$$\Theta \equiv \int_A \int e^{2i\kappa_0 [\alpha x + \beta y + \gamma h(x,y)]} dx dy . \quad (10)$$

The expectation value of the square of the pressure is $\langle PP^* \rangle$, where $*$ denotes the complex conjugate. The random variable that one averages over is the height of the rough surface $h(x,y)$. This expectation value can be written as

$$\langle PP^* \rangle = Q Q^* \langle \Theta \Theta^* \rangle . \quad (11)$$

We define $\langle \Theta \Theta^* \rangle$ as the "rough-surface form function" because it contains all the information on the surface geometry and roughness (i.e., the extrinsic ice properties) and controls the angular dependence of the acoustic return.

$$\langle \Theta \Theta^* \rangle = \iint_A \iint_A e^{2i\kappa_0[\alpha(x-x') + \beta(y-y')]} \langle e^{2i\kappa_0[h(x,y) - h(x',y')]} \rangle dx dy dx' dy'. \quad (12)$$

The standard expectation-value manipulations start with assuming a Gaussian distribution for rough-surface height. This allows one to write

$$\langle e^{2i\kappa_0[h(x,y) - h(x',y')]} \rangle = e^{-2\kappa_0^2 r^2 D(r)}. \quad (13)$$

Here,

$$D(r) \equiv \langle [h(r) - h(r' + r)]^2 \rangle \quad (14)$$

is called the structure function (Ishimaru, 1978). We define $r \equiv (x,y)$ and $r' \equiv (x',y')$.

The structure function gives the square of the average relative vertical displacement of a surface between two points.

We have sparse data (Fig. 4) that are consistent with using a power law to describe the one-dimensional wavenumber spectrum W_1 of the ice surface. These high-wavenumber data are taken from observations by Garrison et al. (1990) of the surface deviation of an ice block (one not used for the acoustics experiment). They were analyzed assuming that the roughness is isotropic. They represent the spectrum for one piece of first-year arctic sea ice. As such, it can be considered a single realization of a one-dimensional wavenumber spectrum, rather than an average spectrum. We use it as a starting point for our theoretical analysis.

A rough surface whose wavenumber spectrum follows a power law can be described as a stationary increment process, where $h(r) - h(r' + r)$ is statistically sta-

tionary. This implies that there is no well-defined rms height deviation of an infinite surface with this kind of spectrum. The rough surface is characterized by a range of horizontal length scales. Jackson et al. (1986) give a formalism that relates the structure function to the two-dimensional, isotropic power-law wavenumber spectrum of the rough surface, $W_2(\kappa)$. They further relate that to the one-dimensional wavenumber spectrum $W_1(\kappa)$, based on work by Ishimaru (1978). Here, we will only quote the results.

If one measures the one-dimensional spectral amplitude η_1 and exponent p_1 of the one-dimensional spectrum

$$W_1(\kappa) \equiv \eta_1 \kappa^{-p_1}, \quad (15)$$

one can relate η_1 and p_1 to the two-dimensional power law wavenumber spectrum $W_2(\kappa)$:

$$W_2(\kappa) \equiv \eta_2 \kappa^{-p_2} \quad (16)$$

with

$$\eta_2 \equiv \eta_1 \frac{\Gamma(\frac{p_2}{2})}{\pi^{1/2} \Gamma(\frac{p_2 - 1}{2})}, \quad (17)$$

where $p_2 = p_1 + 1$.

With this expression for W_2 in terms of η_1 and p_1 , we can solve for the structure function

$$D(r) \equiv C^2 \eta_2 [X^2 + Y^2]^q, \quad (18)$$

where $X \equiv x - x'$, $Y \equiv y - y'$, and

$$C^2 \equiv \frac{2\pi\Gamma(2-q)2^{-2q}}{q(1-q)\Gamma(1+q)}, \quad (19)$$

where $q \equiv (p_2/2) - 1$.

We now have an expression for the rough-surface form function for Kirchhoff theory in the Fraunhofer approximation.

$$\langle \Theta \Theta^* \rangle = \iint_A \iint_A e^{2i\kappa_0(\alpha X + \beta Y) - 2\eta_2 r^2 \kappa_0^2 C^2 (X^2 + Y^2)^q} dx dy dx' dy'. \quad (20)$$

We transform to a circular coordinate system, which reflects the symmetry of the scatters considered.

$$\frac{x}{a} = r \cos \theta \quad ; \quad \frac{y}{a} = r \sin \theta \quad ; \quad \frac{x'}{a} = r' \cos \theta' \quad ; \quad \frac{y'}{a} = r' \sin \theta' \quad (21)$$

for r and r' between 0 and 1, and θ and θ' between 0 and 2π .

We also nondimensionalize this integral expression, which produces three nondimensional parameters,

$$\zeta \equiv \kappa_0 a, \quad (22)$$

$$\eta \equiv \eta_2 a^{2(q-1)} = \eta_2 a^{p_2 - 4} = \eta_2 a^{p_1 - 3}, \quad (23)$$

and p_1 .

We define Ξ and Ω as

$$\Xi \equiv \frac{x - x'}{a} \quad (24)$$

and

$$\Omega \equiv \frac{y - y'}{b}, \quad (25)$$

making use of the transformation from rectangular to circular coordinate systems as described above. We can also nondimensionize the power-law spectrum:

$$W_2(\kappa a) \equiv \eta(\kappa a)^{-p_2}. \quad (26)$$

With these parameters, we write $\langle PP^* \rangle$ as follows:

$$\begin{aligned} \langle PP^* \rangle &= \left[\frac{BRf(\theta_i)\kappa_0}{2\pi |\vec{r}_0| |\vec{r}_1|} a^2 \right]^2 \\ &\times \int_0^1 \int_0^{2\pi} \int_0^{2\pi} e^{2i\zeta(\alpha\Xi + \beta\Omega) - 2\eta\gamma^2\zeta^2 C^2(\Xi^2 + \Omega^2)} rr' dr d\theta dr' d\theta'. \end{aligned} \quad (27)$$

Removing the propagation factors and source level produces the target strength:

$$TS = 10\log(\langle PP^* \rangle) + 20\log(|\vec{r}_0| |\vec{r}_1|) - 20\log(B). \quad (28)$$

Remember that in these expressions α , β , and γ are simply geometrical quantities.

Also, note that the rough-surface acoustic return is dependent on the size of the object beyond the usual considerations of the area of the object and ζ : the effects of the size on the total backscatter also come in through the parameter η .

Analysis of the rough surface form function—effects of η , p_1 , and ζ near their "observed" values

We will now show how the normalized form function given by the integral in Eq. (27) varies with ζ , η , and p_1 near the values suggested in Fig. 4. These parameters are the normalized acoustic wavenumber, spectral amplitude, and the exponent of the one-dimensional wavenumber spectrum, respectively.

Note that ζ is the standard nondimensional parameter from the problem of diffraction through a circular aperture. It appears in both the oscillating and damping exponentials in the integrand. For $\eta = 0$ and a constant p_1 , we will obtain the standard oscillating form function, which is $[J_0(X)/X]^2$ for round scatterers, where $X = 2\zeta \sin\theta$ (Goodman, 1968).

We first consider the angular dependence of the rough surface form function for a constant but nonzero η , a constant p_1 , and increasing ζ . The number of lobes will increase as for a smooth square. However, the damping exponential in the integral of (27), whose argument is proportional to ζ^2 , will reduce the amplitudes of the lobes and fill in the valleys of the form-function pattern. The mathematical expression shows this directly. We also demonstrate this smoothing out of the form function in Fig. 5, which shows the near-normal-incidence pattern for a fixed value of η and p_1 and a range of ζ , all corresponding to the arctic experiments. By $\zeta = 97$, the lobe and valley patterns are completely smoothed over.

FIG 5

We now consider holding both ζ and p_1 fixed and varying the spectral strength of the rough surface via η (Fig. 6). This also leads to rough-surface form functions with lobes and valleys that are smoothed over as η increases. As the surface roughness increases, more energy is kicked out from the ice block away from normal incidence. This is due to the damping term in the integral in Eq. (27), which is dependent on η . For increases in either ζ or η , the main lobe of the rough-surface form function tends to widen and decrease in level.

Figure 7 shows the rough-surface form function for a range of p_1 , for fixed η and ζ . The functional dependence of the rough-surface form function is more subtle than it would first appear. The smallest value of p_1 gives a net lower return than the larger two values. This is due to the larger high frequency contributions to the rough surface at this value of p_1 . This increase in high frequency contributions for smaller p_1 occurs because of the relatively shallow tilt of the power law spectrum, as well as a general increase in the value of the spectral strength (η_1 , within η) relative to the other two values of p_1 for a constant value of η . The case of $p_1 = 1.8$ is more coherent than that of $p_1 = 2.8$ because of the way the parameter p_1 works within η . Equation (23) shows that once $3 - p_1 < 1$ for increasing p_1 and a constant value of η , then η_2 hence η_1 has to increase quickly relative to continued increases in p_1 in order to keep η constant. An increase in the dimensional spectral strength produces a rougher surface, with an increase in the strength of the wavenumber spectrum of the ice surface that more than compensates for

the relative decrease in the high frequency components of the roughness spectrum as p_1 increases beyond 2.

Competing with the decrease in returns due to increased ζ and η or (generally) decreased p_1 will be a rise in target strength due to the κ_0^2 dependence shown in Eq. (27). The observed reduction of the reflection coefficient as frequency increases supports the decrease in target strength (see below).

INITIAL COMPARISON OF THEORY AND DATA

To compare the theory [Eq. (28)] with the experimental data (Fig. 2), we describe the reflection coefficient used. For a perfectly flat, infinite interface, it is well known (Bass, 1958) that the acoustic return at normal incidence is a replica of the transmitted pulse whose amplitude is affected by the reflection coefficient. For a rough interface, it can be shown (Melton and Horton, 1970; McDonald and Spindel, 1971; Thorsos, 1984) that if the beamwidth of the transmitter/receiver is larger than the angular width of the normalized backscattering cross section, and if the pulse length is long enough so that returns from all regions within the beamwidth overlap, the amplitude of the ensemble average of the returns from the rough interface will be the same as the amplitude for the equivalent flat interface. Thus an ensemble of returns meeting these conditions allows determination of the intrinsic reflection coefficient R in Eq. (27). Figure 8 shows amplitude reflection coefficients determined from ensemble measurements of normal-incident scattering off the ice canopy. Only the data taken with the ITC 1042 transducer, which is

Fig
8

omnidirectional, fulfill the transmitter/receiver conditions given above. The other data were taken with directional transmitters/receivers, but the beamwidths were large enough below 80 kHz that the values should not be affected significantly (Francois et al., 1989). In evaluating our expression for the target strength, Eqs. (27) and (28), we will first use the parameterization for $R(f)$ shown as a dotted line in Fig. 8.

Our interpretation of the physics controlling the data in Fig. 8 is based on an analysis begun by D. Winebrenner (personal communication, 1991). His work, in its most general form, is an extension of results presented by Brekhovskikh (1980), among others, for reflection from a smooth interface backed by continuously varying, compressional sound speed and density profiles. Winebrenner extended this by adding variable attenuation and calculating the jump produced in the reflection coefficient by a discontinuity in the sound speed and/or density profiles. Francois et al. (1989) and Mourad et al. (1990) presented an unpublished analysis by Mourad and Winebrenner showing in detail the case of constant ice density and no attenuation, which is equivalent to the formalism presented by Brekhovskikh (1980). Figure 9 shows a hypothetical sound speed profile of form

$$c(z) = \begin{cases} c_0 & \text{if } z < 0 \\ 2[c_i - (c_1)/2] + (c_1 - c_i)[1 + \tanh(\delta z)] & \text{if } z \geq 0 \end{cases} \quad (29)$$

for $\delta = 10^5 \text{ m}^{-1}$. Here, c_0 is the sound speed in the water, c_i is the sound speed in the ice at the ice/water interface, and c_1 is the bulk sound speed (i.e., the compressional-wave

sound speed in the interior of the ice). The values used for these parameters are shown in Fig. 10. Measurements of actual compressional-wave sound speed profiles are hard to come by because of the high porosity of the skeletal layer, which makes it difficult to handle the ice while maintaining its *in situ* properties (Williams and Francois, 1991). Bogorodskii et al. (1975, 1976) report large gradients in sound speed within the slushy skeletal layer.

FIG 10

The theoretical, frequency-dependent reflection coefficient calculated for this sound speed profile is given by the solid line in Fig. 10. For this calculation, we chose $\rho_{\text{ice}}/\rho_{\text{water}} = 0.95$. The low frequency limit of this reflection coefficient is $R = 0.43$, which can be shown by the thin-layer theory presented by Brekhovskikh (1980).

At low frequencies, the reflection coefficient is determined by the bulk impedance mismatch between the ice and water; essentially, the skeletal layer is too thin to have a significant effect on the apparent reflectance of the ice. At high frequencies, the sound speed gradient is too weak to reflect acoustic energy back into the water; consequently, the reflection coefficient is determined by the surface impedance mismatch. Because of uncertainty about the sound speed gradient in the skeletal layer, more direct measurements are needed to quantify the theory.

Using the equation for the reflection coefficient from Fig. 8 and the spectrum of Fig. 4, we can make a comparison between theoretically predicted *average* returns and measured *individual realizations* for a recently submerged ice block.

Figure 11 shows this comparison as a function of incidence angle for the ice/water interface of submerged ice blocks. For 20 kHz, the model-data comparison is plausible, including the minor smoothing of the lobes and valleys of the predicted average pattern relative to the smooth surface result. However, there are much larger differences between average predictions and the individual realizations for the 40 and 80 kHz data.

We have used our best guess at observed inputs for the theory, understanding that the spectral inputs were particularly problematic, since they were obtained from an individual realization of a piece of ice that was different from the one used for the acoustic experiments. That comparison suggests the measured spectrum was too rough compared with the spectrum from the ice block used for the acoustics experiments. We will therefore turn the analysis around, using the theory to predict spectral strengths and exponents, and the sound speed structure within the skeletal layer of the ice used for the acoustic experiment. We do so considering a wider range of parameter values, reflecting a larger choice of rough surface wavenumber spectra and sound speed profiles. The main difficulty with this approach is the fact that we only have predictions of average target strength and observations of individual realizations of target strength, a process that becomes more random as frequency increases.

SECOND COMPARISON: PREDICTION OF PHYSICAL PARAMETERS USING EXPERIMENTAL DATA AND ENSEMBLE THEORY

Figure 12 shows the rough-surface form functions calculated for normal-incidence backscatter from a block with a range of spectral strengths and exponents and over a range of frequency (ζ with constant block size $a = 0.29$ m). The rate at which the form function diminishes as frequency increases depends on both η and p_1 . For example, when there is a larger high-frequency component to the spectrum (large η and small p_1), the rough-surface form function falls precipitously as f increases. (We shall see that in this case the acoustic returns rapidly become incoherent for increasing frequency.) Where there is a smaller high-frequency component to the rough surface spectrum (when η is relatively small and p_1 is relatively large), the normal-incidence, rough surface form function drops off more gently with increasing ζ . Also note that there are larger changes in the rough-surface form function, hence in target strength, at large frequencies compared with small frequencies. This means that the large frequency results will be more sensitive to the shape of the rough surface spectrum than the low frequency results and will therefore be a better indicator of the rough surface statistics.

Figure 12 can be used to develop an estimate of the target strength of large blocks of ice, in concert with Eq. (28), if one has a good estimate of η_1 (hence η_2) and p_1 . Calculate η with these values and the radius of the piece of ice in question. Then, read the normal incidence value of the form function from Fig. 12, extrapolating where necessary.

Fig
12

Use this value in combination with the appropriate multiplicative factors in Eq. (27) to calculate the target strength at normal incidence.

Figure 13 shows the predicted average target strength at 20 kHz, for a range of p_1 and η , using the average reflection coefficient listed in Fig. 8. The return is less coherent for small p_1 and large η than for large p_1 and small η . (Comparing the case of $p_1 = 2.8$ versus $p_1 = 2.95$ shows the effect we discussed earlier—Fig. 7.) The best fit of the predictions with the individual realization is centered on values of p_1 and η that suggest a surface smoother than the one measured by Garrison et al. As shown here and in Fig. 12, this low frequency case does not let us adequately bound the rough surface statistics. This is not surprising, since the observed target strength at 20 kHz appears to be made up primarily of coherent acoustic energy, as evidenced by its coherent angular structure.

Figure 14 shows the target strength as a function of incidence angle and a range of p_1 and η , for 80 kHz. As predicted from Fig. 12, there is a large range in level and structure of the target strength for this high frequency case and these different parameter values. The cases of small p_1 and large η completely lose their angular structure compared with the large p_1 and small η cases. With an increase in p_1 for a fixed η up through $p_1 = 2.8$, the normal incidence return increases and the return from outlying angles decreases -- all while the target strength becomes more coherent. This same trend occurs for a decrease in η for fixed p_1 . Comparing the case of $p_1 = 2.8$ vs $p_1 = 2.95$ shows the effect we discussed earlier (Fig. 7).

FIG. 13

FIG. 14

To make the predicted averages come close to the individual realization of target strength, we have chosen a reflection coefficient that is twice the parameterized value. In doing so, we are assuming that the potential difference between the predicted average level and the individual realization at normal incidence is determined entirely by the actual sound speed structure within the ice via the reflection coefficient. We are also assuming that the overall shape is controlled by the roughness statistics. Closer to the truth is that the acoustic return at normal incidence is in part controlled by the inherent variability between individual realizations of $\langle PP^* \rangle$.

The shapes of the average target strength suggest that a good choice of rough surface spectrum parameters is $p_1 = 2.8$ and $\eta = 3.767 \cdot 10^{-6}$, a smoother surface than the values suggested by the single measurement of the spectrum we had at our disposal. Figure 15 shows the predicted, one-dimensional, rough surface spectrum, along with the "observed" spectrum. (We recalculated our model for the edge-term contributions in the Appendix for these new values of p_1 and η . The edge terms remained insignificant.)

Figure 16 shows our final comparison of predicted, average target strength vs individual realizations of target strength, as a function of frequency. The predicted returns are more coherent than our earlier ones. This seems more in line with the structure of the individual returns shown by Garrison et al. (1991). Note that the low and mid frequency reflection coefficient values we used are eerily consistent with the average values picked out by the recursion relation shown in Fig. 8. This suggests that the average sound speed

F 12. 15

F 16. 16

within the bulk of the ice for this experiment was about equal to the average sound speed associated with the average reflection coefficient, about 3800 m/s. However, we had to use a reflection coefficient at 80 kHz that is double the value suggested by the recursion relation, which predicts that $R(40 \text{ kHz}) > R(80 \text{ kHz})$. This change by a factor of two in the reflection coefficient can simply be the result of the higher variability in overall level of target strength at high frequencies than at low frequencies. It may also mark a change in sound speed structure from that inferred from average reflection coefficients (Figs. 9 and 10).

Figure 17 shows our predicted compressional sound speed profile within the skeletal zone of the ice which produces the average normal incidence reflection coefficient shown in Fig. 18 and is consistent with the reflection coefficients used in Fig. 16 in the model/data comparisons. This sound speed profile is given by the following formula and used in the same way as Eq. (29):

$$c(z) = \begin{cases} c_0 & \text{if } z < 1 \\ \frac{1}{2} [(c_i + c_2) - (c_2 - c_i) \cos\left(\frac{\pi(z-1)}{z_t}\right)] & \text{if } z \geq 1 \\ c_1 & \text{if } z \geq z_t \end{cases} \quad (30)$$

where z_t is the top of the skeletal layer. This acoustic waveguide has sharper boundaries than the profile shown in Fig. 9 and has a larger impedance mismatch at the ice/water interface.

FIG. 17

FIG. 18

The hypothetical reflection coefficient shown in Fig. 18 comes rather close to the particular values needed in our target strength comparisons: (20 kHz, 0.2198); (40 kHz, 0.1683); and (80 kHz, 0.1942). What we find particularly encouraging about the profile derived via this inversion procedure is that it has dimensions similar to that inferred from the large batch of average reflection coefficients shown in Figs. 9 and 10. We predict an acoustical thickness of the skeletal layer (defined as the thickness of the layer from the ice/water interface to the point where the speed is 3500 m/s) to be 3–4 cm, based on both data sets. This is in line with our recent *in situ* experimental measurements of sound speed structure within the skeletal zone (Williams et al., 1992).

CONCLUSIONS

We applied the Kirchhoff approximation to the target strength of backscatter from finite, rough surfaces at near-normal incidence and found it was a useful way to interpret the acoustic returns from finite blocks of arctic sea ice. The analysis breaks up the mean square acoustic return into intrinsic and extrinsic factors. The former represents the effects of material properties of the ice on the acoustic backscatter through the reflection coefficient at normal incidence; the latter represents the effects of the rough surface. Three natural, nondimensional parameters are a product of the analysis: $\zeta = \kappa_0 a$, where κ_0 is the acoustic wavenumber and a is the radius of the ice block; $\eta = \eta_2 a^{p_2 - 4}$, where the constants η_2 and p_2 are the spectral amplitude and spectral exponent of the two-dimensional, isotropic power law that describes the rough surface statistics; and

$p_1 = p_2 - 1$, which is the one-dimensional spectral exponent.

We calculated "rough-surface form functions," the counterpart of smooth-surface form functions, for a range of η , ζ , and p_1 . We showed how the lobes and valleys of the form functions are attenuated and filled in, respectively, as η or ζ increases. The behavior is a little more complicated with variations in p_1 , due to its influence on the dimensional spectral strength within η for constant η . The net effect is that with an increase in the higher frequency components of the roughness spectrum there are more incoherent contributions to the target strength. These effects can produce a change of at least 6 - 10 dB in backscatter at normal incidence when compared with the return from a smooth, finite surface.

For the contribution to total backscatter from the intrinsic ice properties, we sketched previous work on how the normal incidence reflection coefficient for the ice/water interface depends on the sound speed profile created by the skeletal layer in the ice. We showed how the variable sound speed structure within the ice can induce a significant frequency dependence in the reflection coefficient, and thus in the backscattering strength. When these different physical mechanisms are combined, they result in the theoretical expressions for average target strength given in Eqs. (27) and (28). Using average values of the reflection coefficient and "observed" values of spectral strength and exponent, we compared our theory with experimental data obtained by Garrison et al. (1991) on backscatter from the natural ice/water interface of a submerged

block of arctic sea ice. Our theory with these inputs gave poor predictions compared with individual acoustic returns from ice blocks. It is important to realize that this observed spectrum was not from the block used in the acoustic experiment.

We then turned the analysis around, using the comparisons of predicted average target strength with individual realizations of target strength of ice blocks to put bounds on the surface roughness and reflection coefficient. We found that the rough surface statistics inferred from this process described a smoother surface than the one shown in Fig. 4. The frequency dependence of the reflection coefficient at normal incidence was largely in line with average observations, especially at low frequencies. At high frequencies (80 kHz), the comparison suggests that the sound speed profile within the individual ice block used for the experiment is quantitatively similar to the one we have inferred from a large set of average reflection coefficients—especially in its prediction for the acoustical thickness of the skeletal layer, 3–4 cm. The big differences are that the inferred single realization of ice/water interface sound speed is about 500 m/s higher than the predicted average ice/water interface sound speed, and that the skeletal layer is a waveguide with sharper boundaries. These changes may be due to the initial warming of the ice block after its submergence and before the acoustic backscatter measurements were made. However, at 80 kHz there is an unquantified, large variability in the observed target strength as well as a rather incoherent predicted average target strength. Taken together, they suggest potentially large variations among individual realizations of target strength.

at this frequency. Therefore, this inferred sound speed profile is not definitive: the factor of two difference between average and implied reflection coefficient that motivated this profile could easily be subsumed within this variability.

ACKNOWLEDGMENTS

This work was supported by the Office of Naval Research (N00014-91-J-1647) and Office of Naval Technology (N00039-91-C-0072). We would like to thank Darrell Jackson of the Applied Physics Laboratory, University of Washington, for his advice and insight.

REFERENCES

Bass, R. (1958). "Diffraction effects in the ultrasonic field of a piston source," J. Acoust. Soc. Am. **30**, 602-605.

Bishop, G. C., W. T. Ellison, and L. E. Mellberg (1987). "A simulation model for high-frequency under-ice reverberation." J. Acoust. Soc. Am. **82**, 275-286.

Bogorodskii, V.V., V.P. Gavrilov, A.V. Gusev, and V.A. Nikitin (1975). "Measurements of the speed of ultrasonic waves in Bering Sea ice," Sov. Phys. Acoust. **21**, 286-287.

Bogorodskii, V.V., V.P. Gavrilov, and V.A. Nikitin (1975). "Sound propagation in ice crystallized from salt water," Sov. Phys. Acoust. **22**, 158-159.

Brekhovskikh, L. M. (1980). *Waves in Layered Media* (Academic, San Diego), 2nd ed.

Clay, C. S., and H. Medwin (1977). *Acoustical Oceanography: Principles and Applications* (Wiley, New York).

Francois, R. E., K. L. Williams, G. R. Garrison, P. D. Mourad, and T. Wen (1989). "Ice keels I: Intrinsic physical/acoustic properties of sea ice and scattering from ice blocks (U)," *Navy J. Underwater Acoust.* **39**, 1203-1228.

Garrison, G. R., R. E. Francois, T. Wen, and W. J. Felton (1990). "Acoustic reflections from cylindrical blocks of arctic ice, 1988," Applied Physics Laboratory, University of Washington, Technical Report APL-UW TR 88.5, Seattle.

Garrison, G. R., R. E. Francois, and T. Wen (1991). "Acoustic reflections from arctic ice at 15-300 kHz," *J. Acoust. Soc. Am.* **90**, 973-984.

Goodman, J. W. (1968). *Introduction to Fourier Optics* (McGraw Hill, New York).

Ishimaru, A. (1978). *Wave Propagation and Scattering in Random Media* (Academic, New York), Vol. 2.

Jackson, D. R., D. P. Winebrenner, and A. Ishimaru (1986). "Application of the composite roughness model to high-frequency bottom backscattering," *J. Acoust. Soc. Am.* **79**, 1410-1422.

Melton, D. R., and C. W. Horton, Sr. (1970). "Importance of the Fresnel corrections in

scattering from a rough surface. I. Phase and amplitude fluctuations," *J. Acoust. Soc. Am.* **47**, 290-298.

Mourad, P. D., K. L. Williams, R. E. Francois, and G. R. Garrison (1990). "Near-normal incidence scattering from rough, finite surfaces: Kirchhoff theory and data comparison," presented at the 119th meeting of the Acoustical Society of America, Pennsylvania State University.

McDonald, J. F., and R. C. Spindel (1971). "Implications of Fresnel corrections in a non-Gaussian surface scatter channel," *J. Acoust. Soc. Am.* **50**, 746-757.

Thorsos, E. I. (1984). "Surface forward scattering and reflection," Applied Physics Laboratory, University of Washington, Technical Report APL-UW 7-83, Seattle.

Tolstoy, I., and C. S. Clay (1966). *Ocean Acoustics* (McGraw-Hill, New York).

Williams, K. L., and R. E. Francois (1991). "Sea ice elastic moduli: Determination of Biot parameters using in-field velocity measurements." *J. Acoust. Soc. Am.* (submitted).

Williams, K. L., G. R. Garrison, and P. D. Mourad (1992). "Arctic sea ice: experimental examination of growing and newly submerged sea ice with acoustic probing of the skeletal layer." (In preparation for *J. Acoust. Soc. Am.*)

APPENDIX

To examine the contribution of boundary terms of the form discarded in Eq. (1) to obtain Eq. (6), we consider the one-dimensional function [compare with Eq. (5)]

$$f(\theta, \kappa_0, a, h) = \frac{\alpha}{2i\kappa_0\gamma} e^{2i\kappa_0[\alpha x + \gamma h(x)]} \left[\int_{-a}^a - \int_{-a}^a \frac{\alpha^2}{\gamma} e^{2i\kappa_0[\alpha x + \gamma h(x)]} dx - \int_{-a}^a \gamma e^{2i\kappa_0[\alpha x + \gamma h(x)]} dx \right], \quad (A1)$$

where the variables are as defined in the body of the article. Calculating the expectation value of this expression gives

$$\langle ff^* \rangle = t1 + t2 + t3 \quad (A2)$$

where

$$t1 = -\frac{\tan^2 \theta}{2\kappa_0^2} \left[1 - \cos(4\kappa_0\alpha a) e^{-2\kappa_0^2\gamma^2 D_1(2a)} \right], \quad (A3)$$

$$(A4)$$

$$t2 = -\frac{\tan \theta}{\kappa_0 \cos \theta} \left(\int_{-a}^a \sin[2\kappa_0\alpha(a-x)] e^{-2\kappa_0^2\gamma^2 D_1(a-x)} dx + \int_{-a}^a \sin[2\kappa_0\alpha(-a-x)] e^{-2\kappa_0^2\gamma^2 D_1(-a-x)} dx \right),$$

and

$$t3 = \frac{1}{\cos^2 \theta} \left(\int_{-a}^a \int_{-a}^a [e^{2i\kappa_0 \alpha (x-x')}] e^{-2\kappa_0^2 \gamma^2 D_1(x-x')} dx dx' \right). \quad (A5)$$

We are considering backscattering here, where $\theta \equiv \theta_0$. Also, D_1 is the one-dimensional structure function which can be calculated using the one-dimensional spectrum in Eq. (15), giving

$$D_1(x) = \frac{2\eta_1}{\left[\frac{1}{2}(p_1-1)(p_1-2) \right]} \Gamma(3-p_1) \cos\left[\left(\frac{3}{2} - \frac{p_1}{2}\right)\pi\right] (x^2)^{\frac{p_1-1}{2}}. \quad (A6)$$

If the first term in Eq. (A1) is discarded, the expectation value in Eq. (A2) is equal to $t3$, a one-dimensional version of the term retained in the body of this paper for our theory. Figure A1 shows the relative magnitude of $t1$, $t2$, and $t3$ as η_1 is varied. The parameter values are as follows: $\kappa_0=174.5$, $a=0.29$, and $p_1 = 1.8$, which are representative of some of the values we used in this article. For these near-normal angles, one sees that the boundary term contributions $t1$ and $t2$ are indeed small relative to $t3$ and can be discarded with negligible effect.

Figure Captions

FIG. 1. Elevation view of experimental arrangement for the ice-block experiment performed by Garrison et al. (1991).

FIG. 2. Comparisons of the theoretical and measured target strengths of a circular, air-filled pan (left panel) and of the theoretical return from a smooth circular disc and individual returns measured from the bottom of a submerged cylinder of arctic sea ice (right panel). Details are given by Garrison et al. (1991).

FIG. 3. Coordinate system for the theory (after Clay and Medwin, 1977).

FIG. 4. "Observed" one-dimensional spectrum of arctic sea ice. The straight-line fit gives $W_1(\kappa) = \eta_1 \kappa^{-p_1}$ for $\eta_1 = 0.0000168$ and $p_1 = 1.8$.

FIG. 5. Comparison of theoretical calculations of rough-surface form functions (solid line) and smooth-surface form functions (dotted line) for parameters close to those observed: $\eta = 1.2557 \cdot 10^{-5}$, $p_1 = 1.8$, $a = 0.29$ m. At $f = 20$ kHz (a), the lobes of the rough-surface pattern are reduced and the valleys are filled in compared with the smooth-surface pattern. At 40 kHz (b), there is more smoothing of the rough-surface form function as incoherent scattering processes become important. At 80 kHz (c), the return is dominated by incoherent scattering, as evidenced by the absence of a beam

pattern for the rough-surface case.

FIG. 6. Effect of η on the rough-surface form function, with other parameters held constant: $\zeta = 24.295$, $p_1 = 1.8$, $f = 20$ kHz, $a = 0.29$ m. This figure shows how an increase in η , our nondimensional form of the one-dimensional spectral strength, causes a reduction in the coherent return from a rough surface, as evidenced by the smoothing of the coherent beam pattern.

FIG. 7. Effect of p_1 on the rough-surface form function, with other parameters held constant: $\zeta = 24.295$, $\eta = 1.2557 \cdot 10^{-5}$, $f = 20$ kHz, $a = 0.29$ m. The general trend is that for decreasing p_1 there is an increase in the incoherent contribution to the total backscatter, hence a reduction in total average backscatter and in its diffraction pattern. See the text for details.

FIG. 8. Observations of average reflection coefficients for the ice/ocean interface, as discussed by Garrison et al. (1990) and references within. The recursion relation (dashed line) is given by $R = 0.45 - 0.18 \log f$, where f is in kilohertz (Francois et al., 1989). Symbols refer to the different transducers used in the experiments.

FIG. 9. Hypothetical sound speed profile used to model the sound speed within the skeletal layer, i.e., within the slushy ice/ocean interface of first-year arctic sea ice (Garrison et al., 1991). This profile was chosen to be consistent with observations of

sound speed within the skeletal layer and to produce a reflection coefficient consistent with observations (Fig. 10).

FIG. 10. Theoretical reflection coefficient calculated for the sound speed profile shown in Fig. 9. The parameter values used in Eq. (28) are noted. For low frequencies, the reflection coefficient is determined by the bulk impedance mismatch (i.e., by the constant value of the sound speed away from the interface). For high frequencies, the reflection coefficient is determined by the discontinuity in sound speed at the ice/water interface. For mid frequencies, there is a transition from one regime to the other.

FIG. 11. Average target strength (solid line) at 20, 40, and 80 kHz predicted by Eqs. (27) and (28) compared with representative observations by Garrison et al. (1991). The dotted line shows the smooth surface prediction, with the normal incidence value chosen to match that of the rough surface predictions. Predicted target strength is displaced to the left by 0.35° in the first two panels and by 0.20° in the bottom panel. Parameter values used in the calculations are $\eta = 3.7679 \cdot 10^{-5}$, $p_1 = 1.8$, $a = 0.29$ m, and those noted in each panel. Both observations and theory show a well-defined beam pattern at 20 kHz, which disappears at higher frequencies. The theoretical predictions do not succeed in producing predicted average target strengths that come plausibly close to the individual realizations of target strength: the levels and shapes are too different.

FIG. 12. Predictions of the normal incidence rough-surface form function -- the

integral in Eq. (27). We vary the frequency (ζ with $a = 0.29$ m, with the actual frequencies noted on the figure) and nondimensional parameters p_1 (the spectral exponent of the one-dimensional rough surface spectrum) and η (the nondimensional rough surface spectral amplitude). The net result is that the rough-surface form function decreases with combinations of p_1 and η that maximize the high wavenumber contributions to the rough surface statistics, and especially quickly at large acoustic frequencies. In the text, we describe a way to infer the target strength of large (round) ice block surfaces, given this figure and knowledge of the rough surface statistics.

FIG. 13. A series of comparisons of predicted target strength at 20 kHz with an individual realization of target strength. Predicted target strength is displaced to the left by 0.35° . The one-dimensional rough surface spectral exponent p_1 and nondimensional spectral strength η are varied in the theory to infer candidate rough surface spectra that would correspond with the observations of target strength. Constant parameters are $\zeta = 24.295$ and $a = 0.29$ m. The reflection coefficient, 0.2128, is chosen from the parameterization in Fig. 8.

FIG. 14. As in Fig. 13, for 80 kHz, $\zeta = 97.159$, $a = 0.29$ m, and a reflection coefficient of 0.1968, twice the value given by the parameterization of Fig. 8. Here the predicted target strength is displaced to the left by 0.20° . Unlike the 20 kHz case, these comparisons of average target strength with an individual realization of target strength more

strongly constrain plausible (p_1, η) pairs.

FIG. 15. Data from one observation of the rough surface spectrum of a piece of undeformed arctic sea ice, its match with a one-dimensional rough-surface power law spectrum (the upper line) and our prediction of the one-dimensional rough-surface power law spectrum based upon analysis of a different piece of ice.

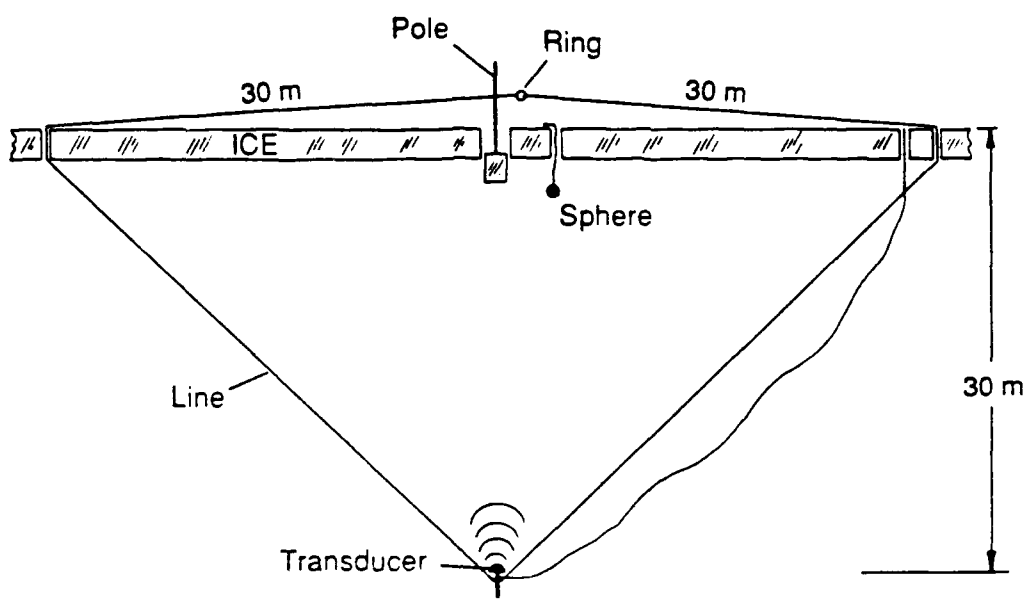
FIG. 16. Final comparison of predicted average target strength (solid line) and individual realizations of target strength (squares), as a function of frequency. The dotted line shows the smooth surface diffraction pattern, with a normal incidence level set to match the predictions. Predicted target strength is displaced to the left by 0.35° in the first two panels, and by 0.20° in the bottom panel. The theoretical inputs are $\eta = 3.7679 \cdot 10^{-6}$, $p_1 = 2.8$, $a = 0.29$ m, and those noted on the figure. The reflection coefficients were chosen to bring the normal incidence, average target strength prediction in line with the observations. The spectral strengths and exponents were chosen to match the trends in angular dependence, specifically the smoothing of the smooth surface diffraction pattern with increasing frequency.

FIG. 17. Predicted sound speed profile within the skeletal layer of the ice, chosen to produce the hypothetical frequency-dependent reflection coefficient shown in Fig. 18 that matches the model inputs used in Fig. 16. This is a prediction, subject to the caveats noted in the text, for the sound speed profile within the ice blocks used in the experiments

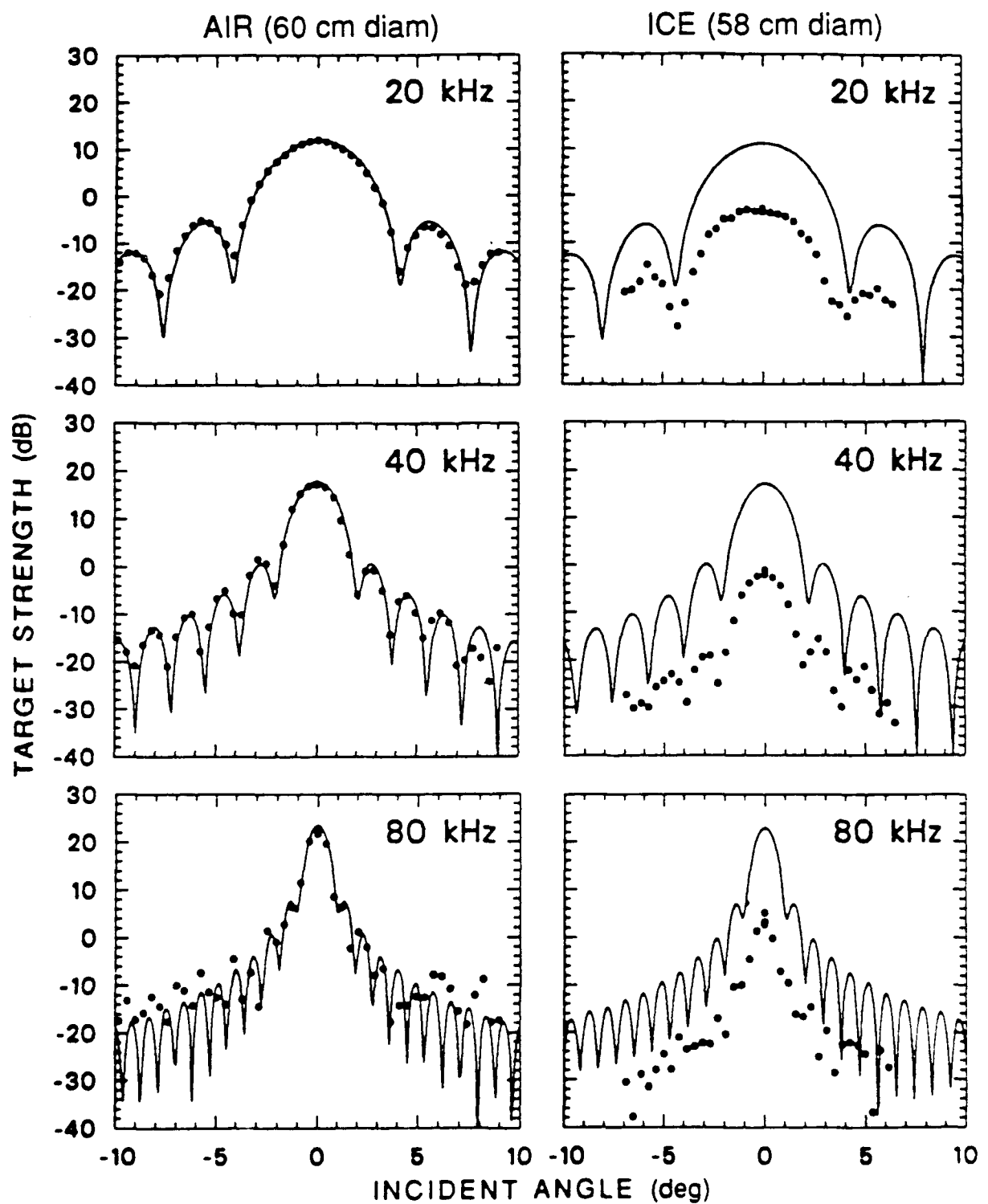
of Garrison et al. (1991). This profile has the same overall structure of the average sound speed structure inferred in Fig. 10 from *average* reflection coefficients, especially the acoustic thickness of the skeletal layer of the ice.

FIG. 18. Predicted frequency-dependent reflection coefficient consistent with the sound speed structure shown in Fig. 17, calculated using the theory of Brekhovskikh (1980) (see text for details).

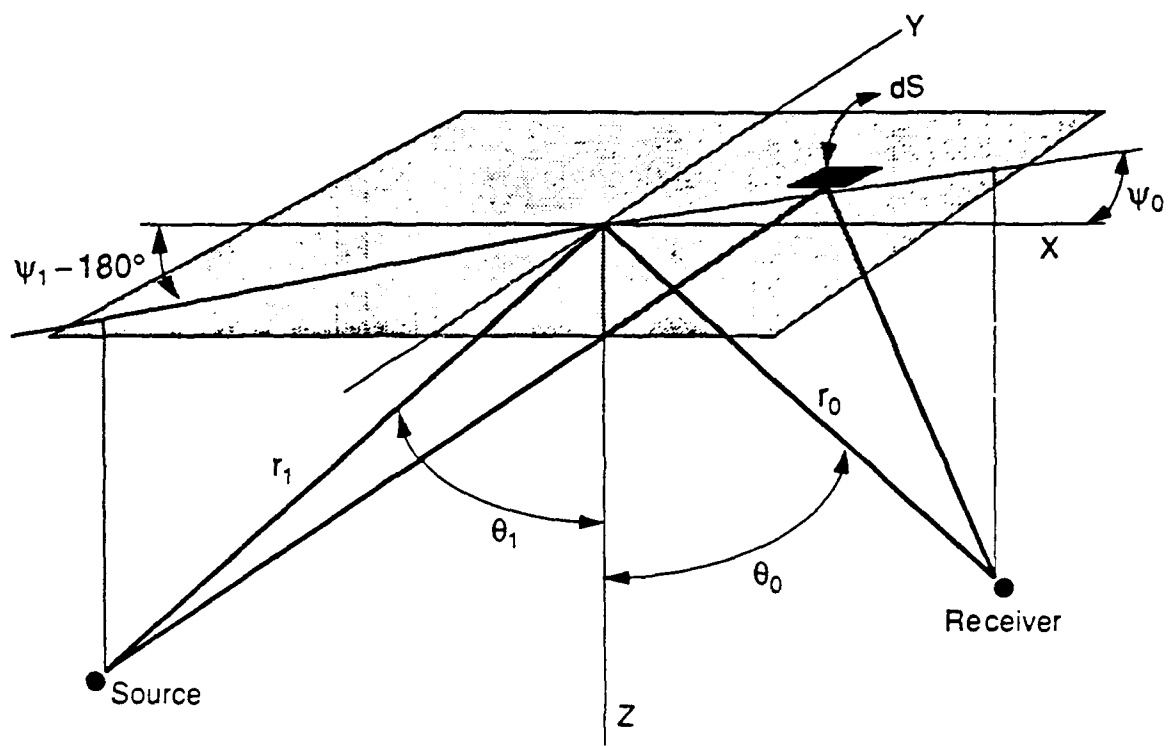
FIG. A1. Comparison of the relative contributions of the boundary terms (t_1, t_2) and the term (t_3) analogous to the one retained in Eq. (6). The parameter values used are as follows: $\kappa_0 = 174.5$, $a = 029$, and $p_1 = 1.8$, with η chosen to bracket the value given in Fig. 4.



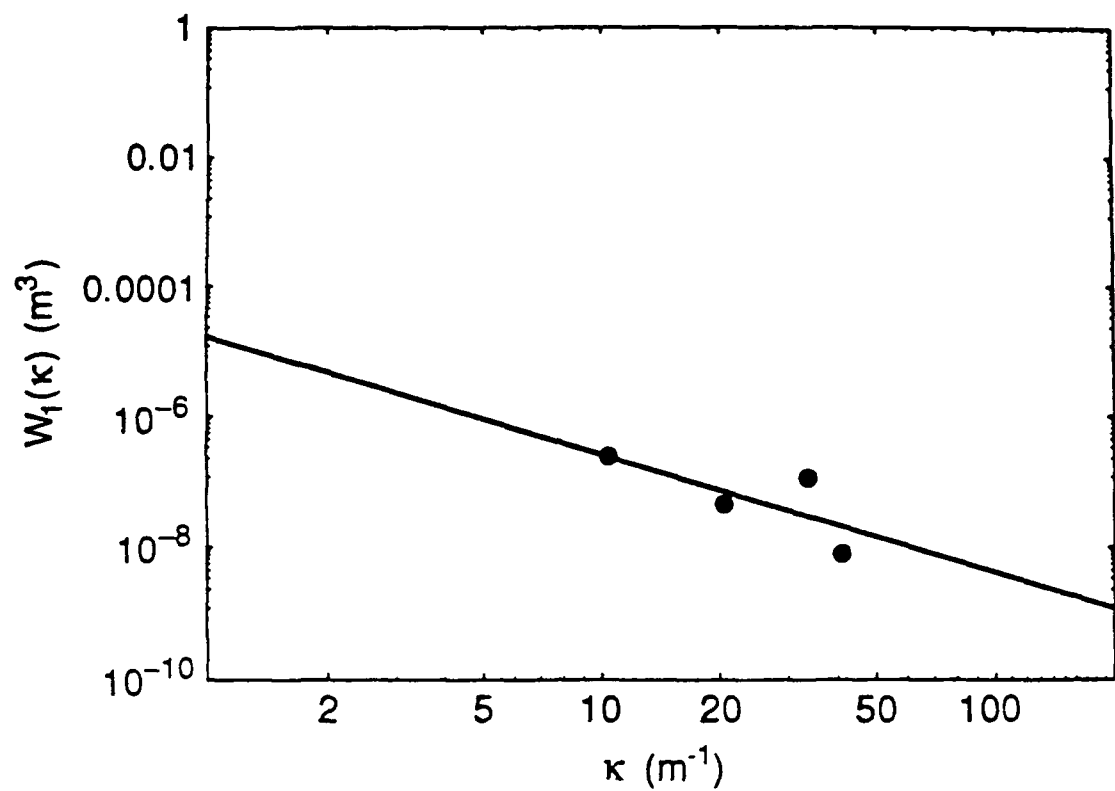
MOURAD, WILLIAMS Fig. 1



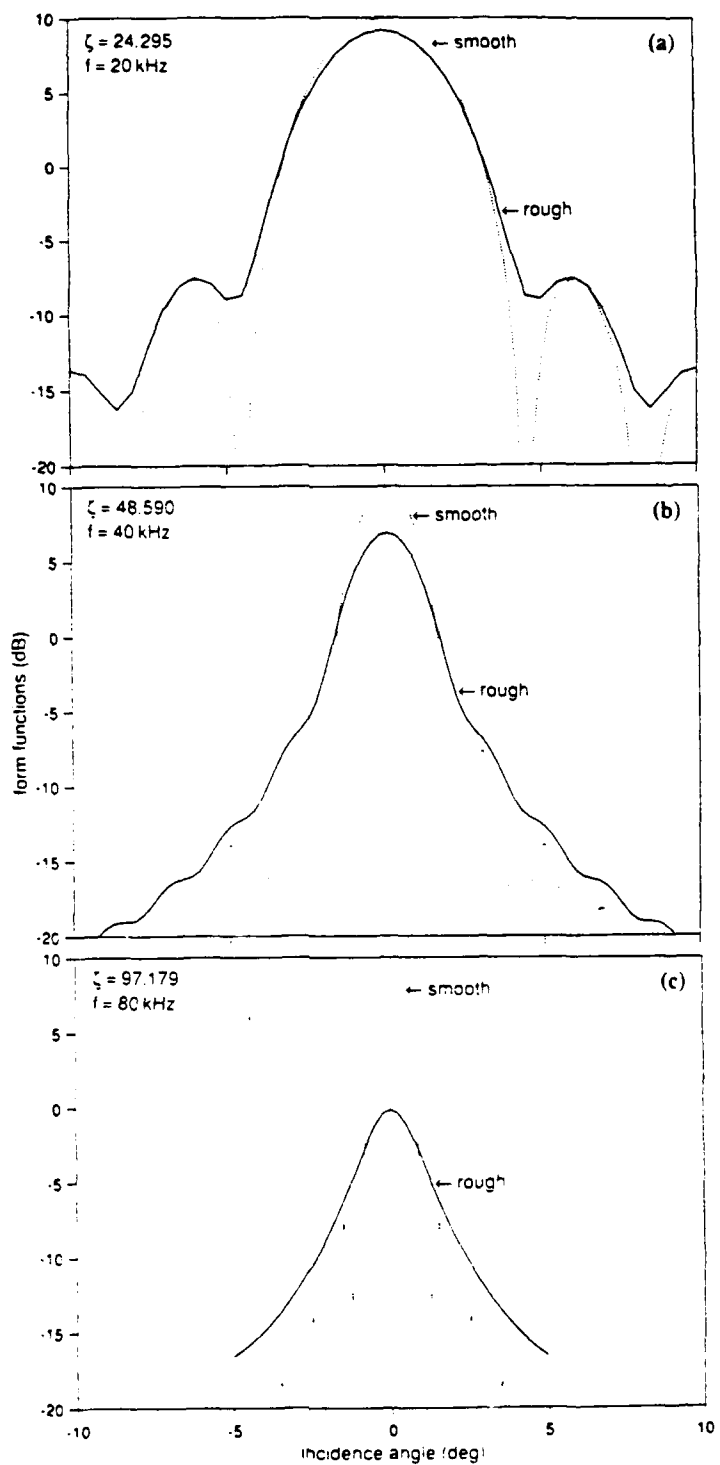
MOURAD, WILLIAMS Fig. 2



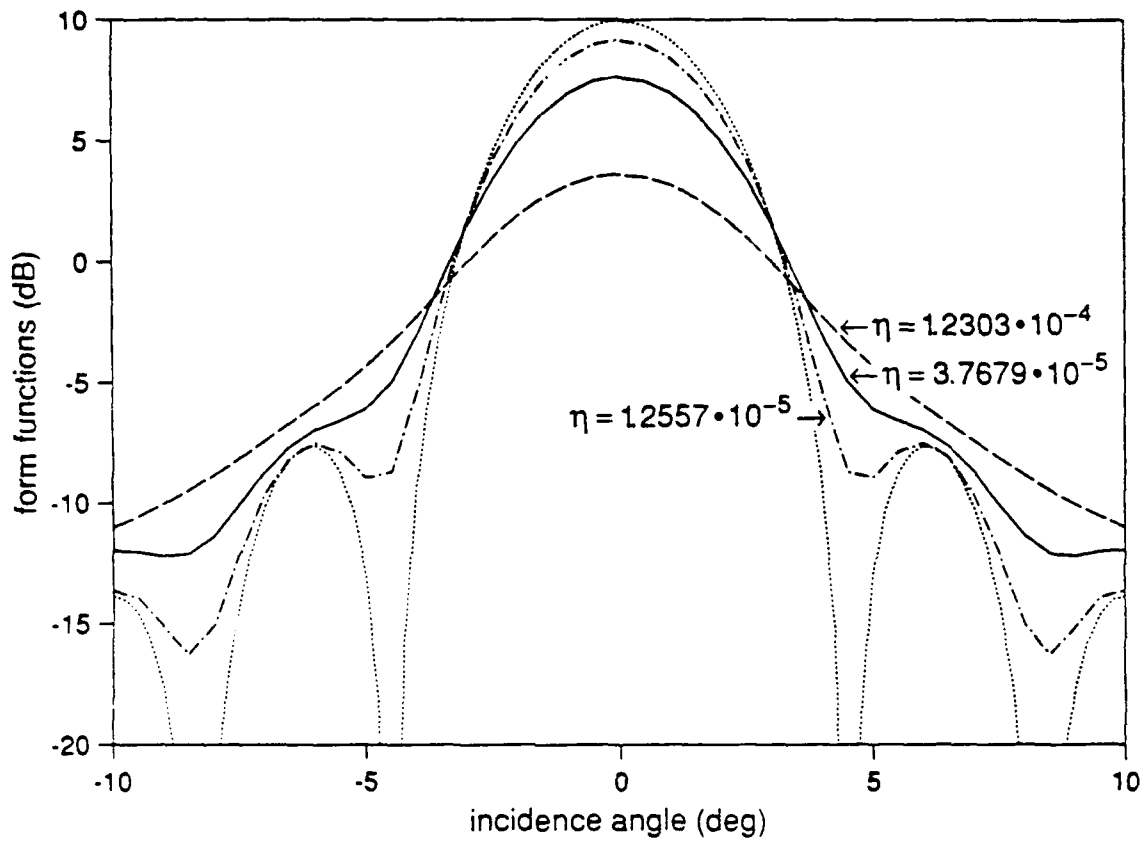
MOURAD, WILLIAMS Fig.3



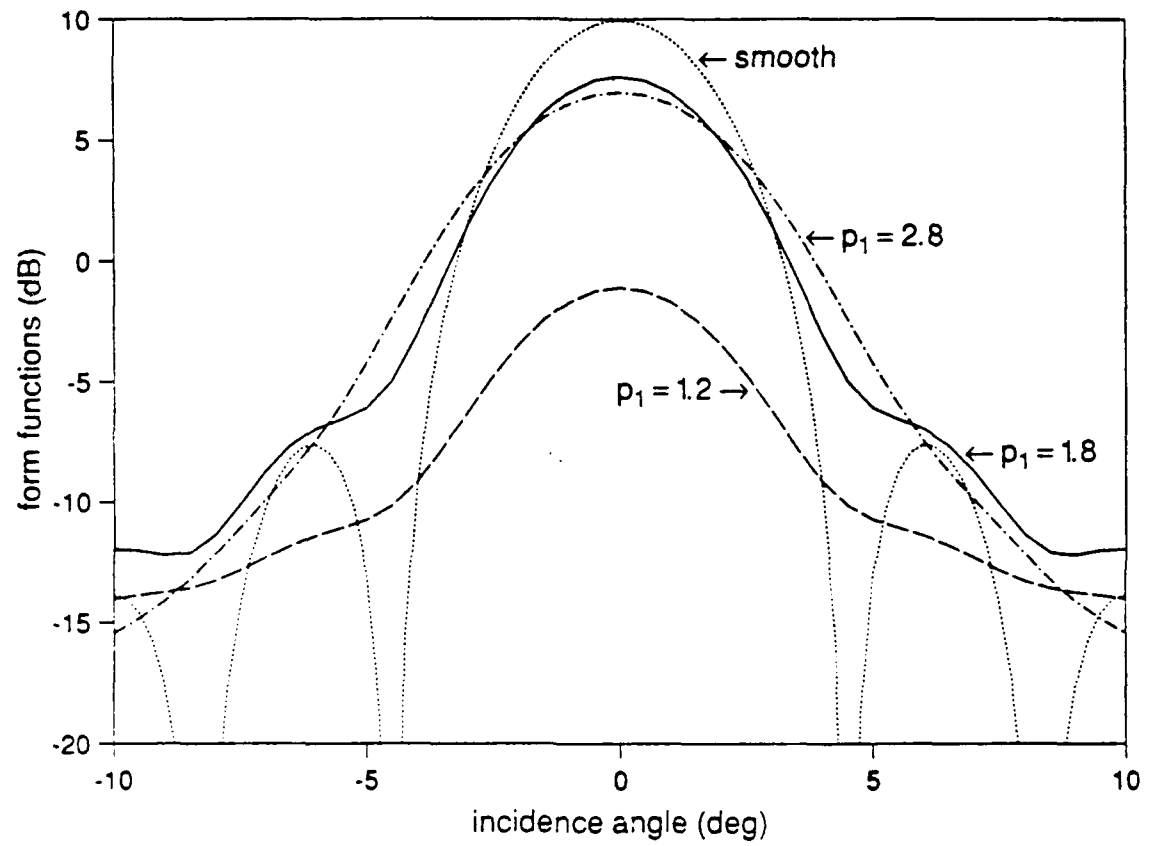
MOURAD, WILLIAMS Fig. 4



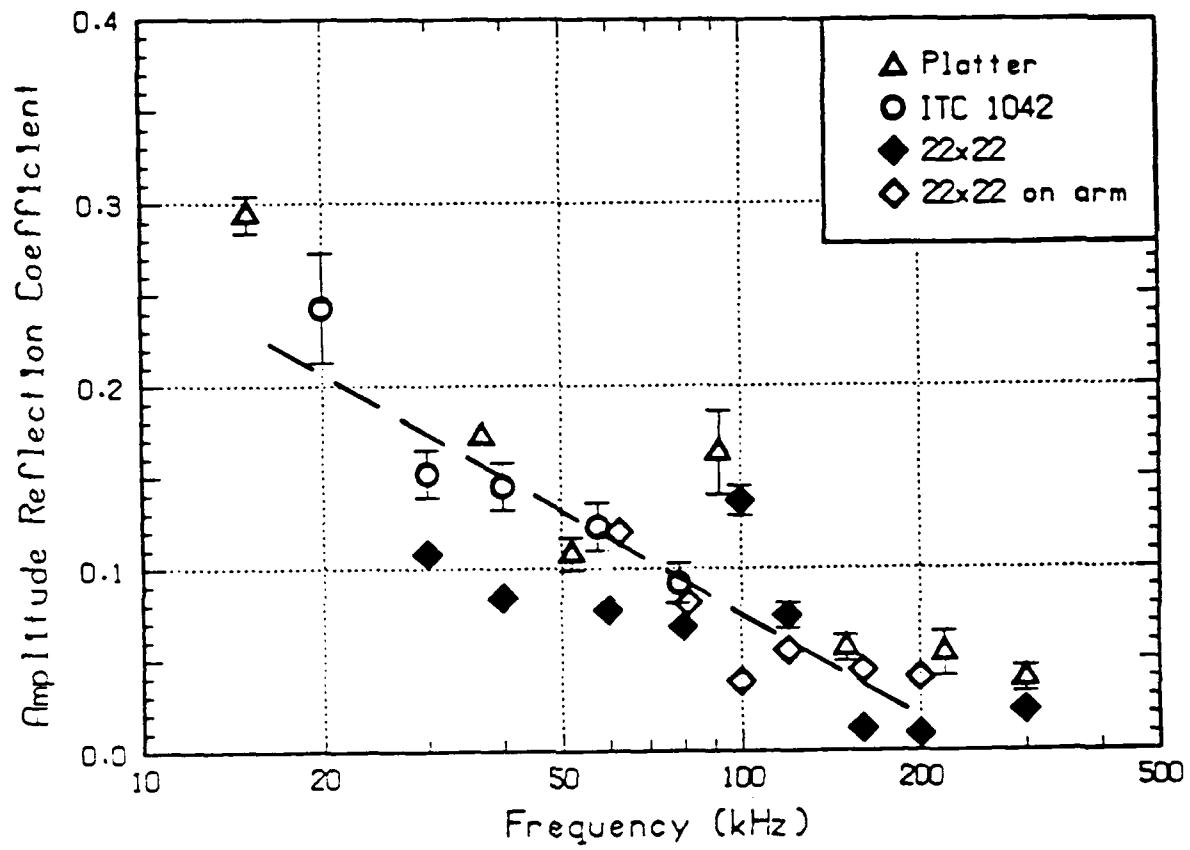
MOURAD, WILLIAMS Fig. 5



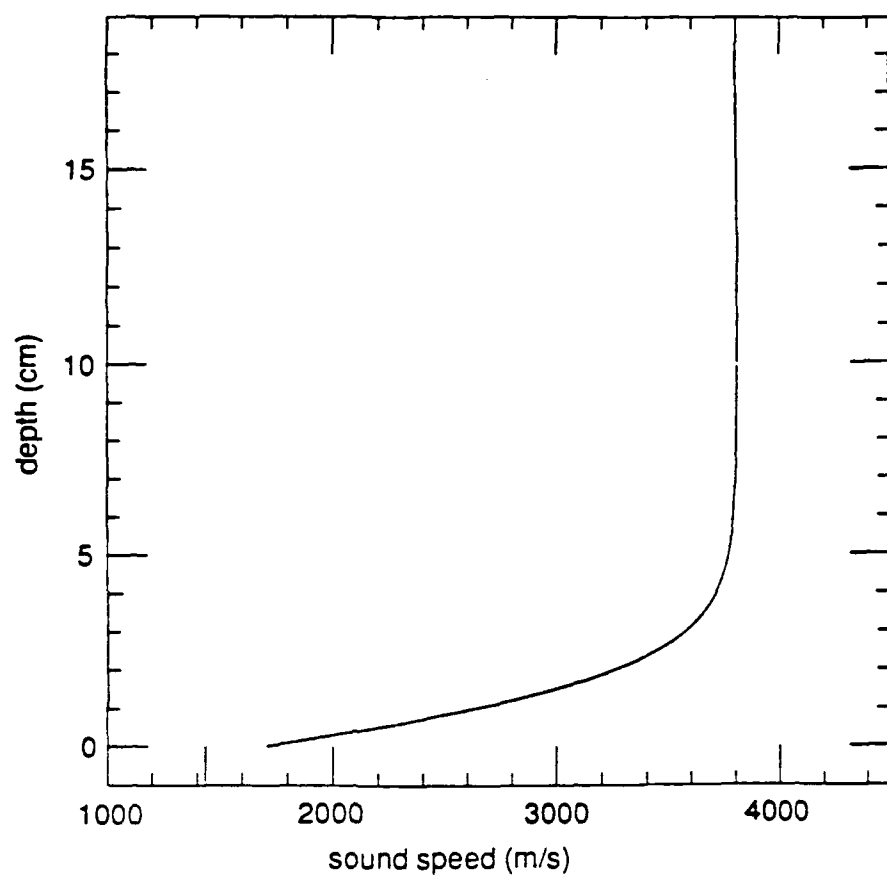
MOURAD, WILLIAMS Fig. 6



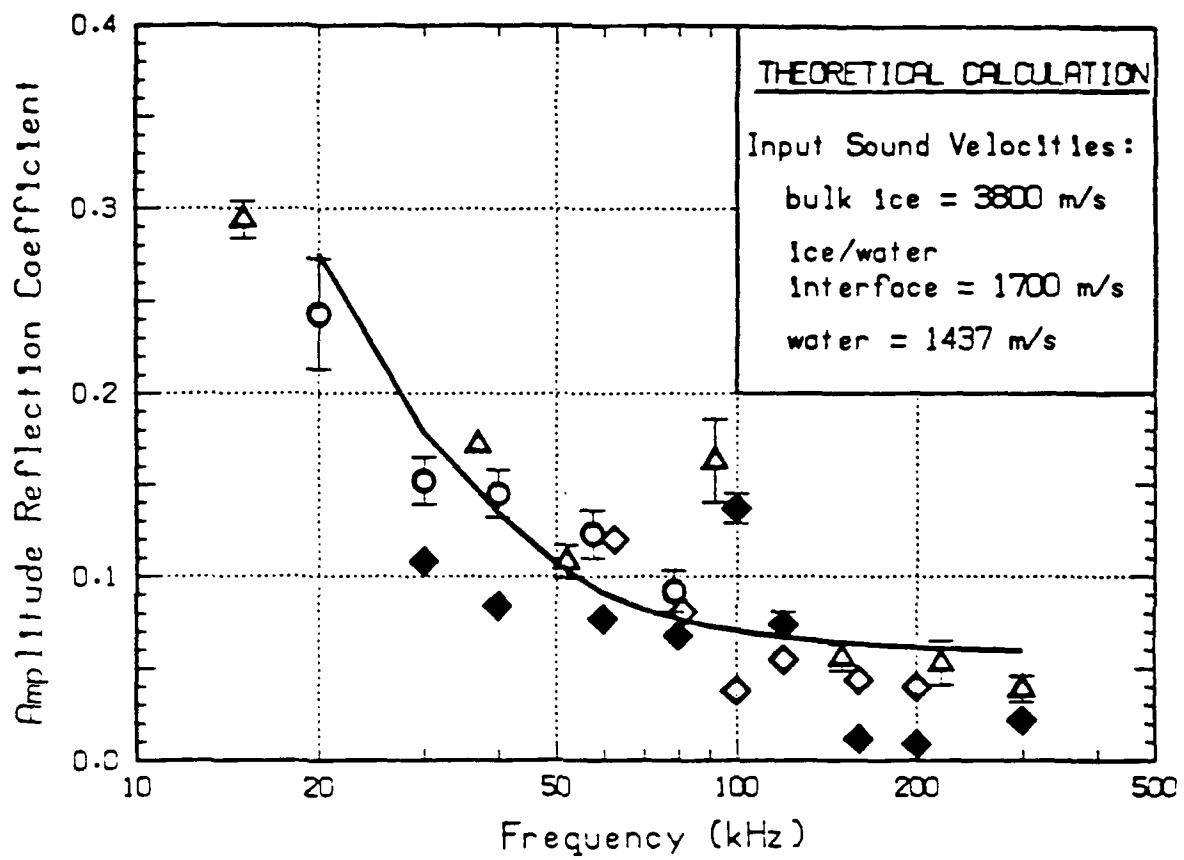
MOURAD, WILLIAMS Fig. 7



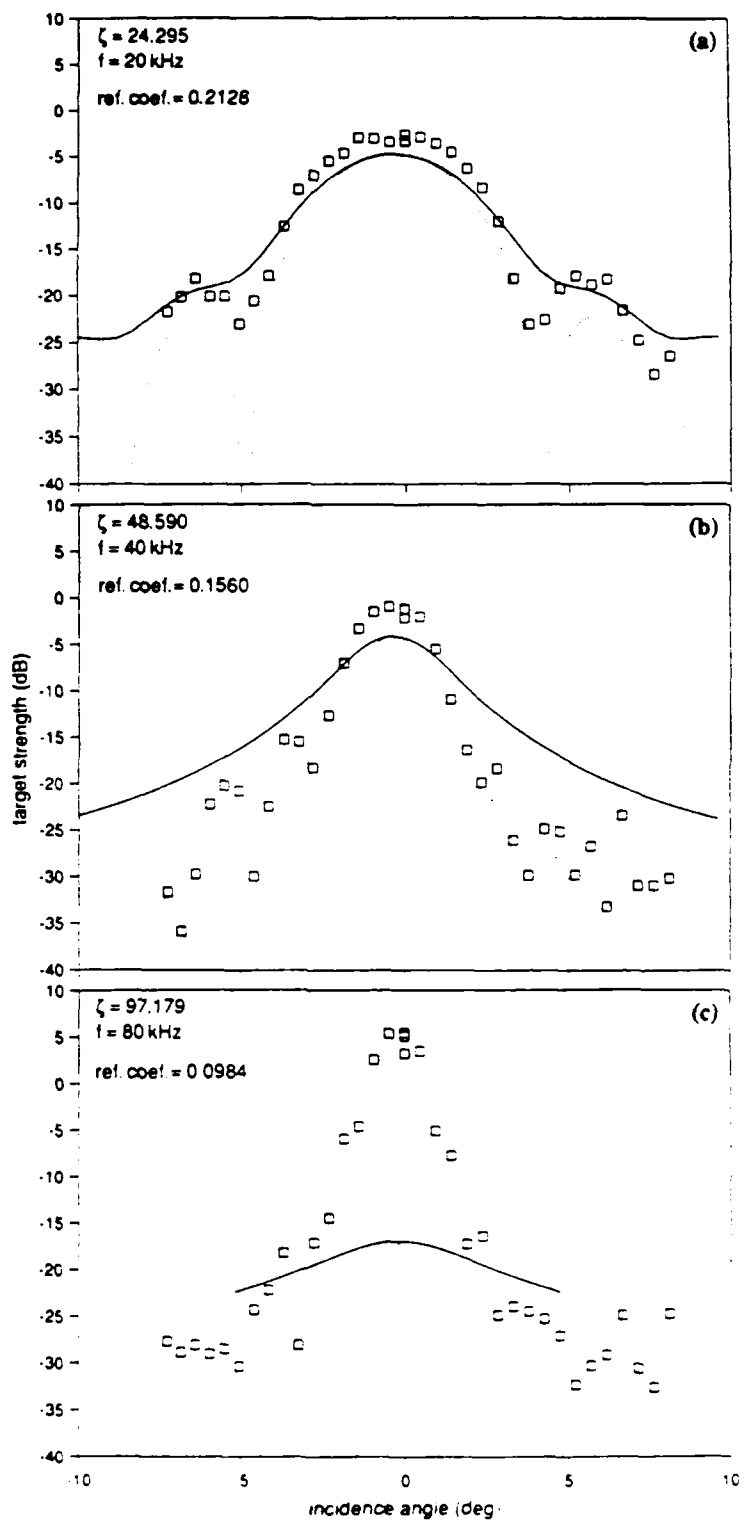
MOURAD, WILLIAMS Fig.8



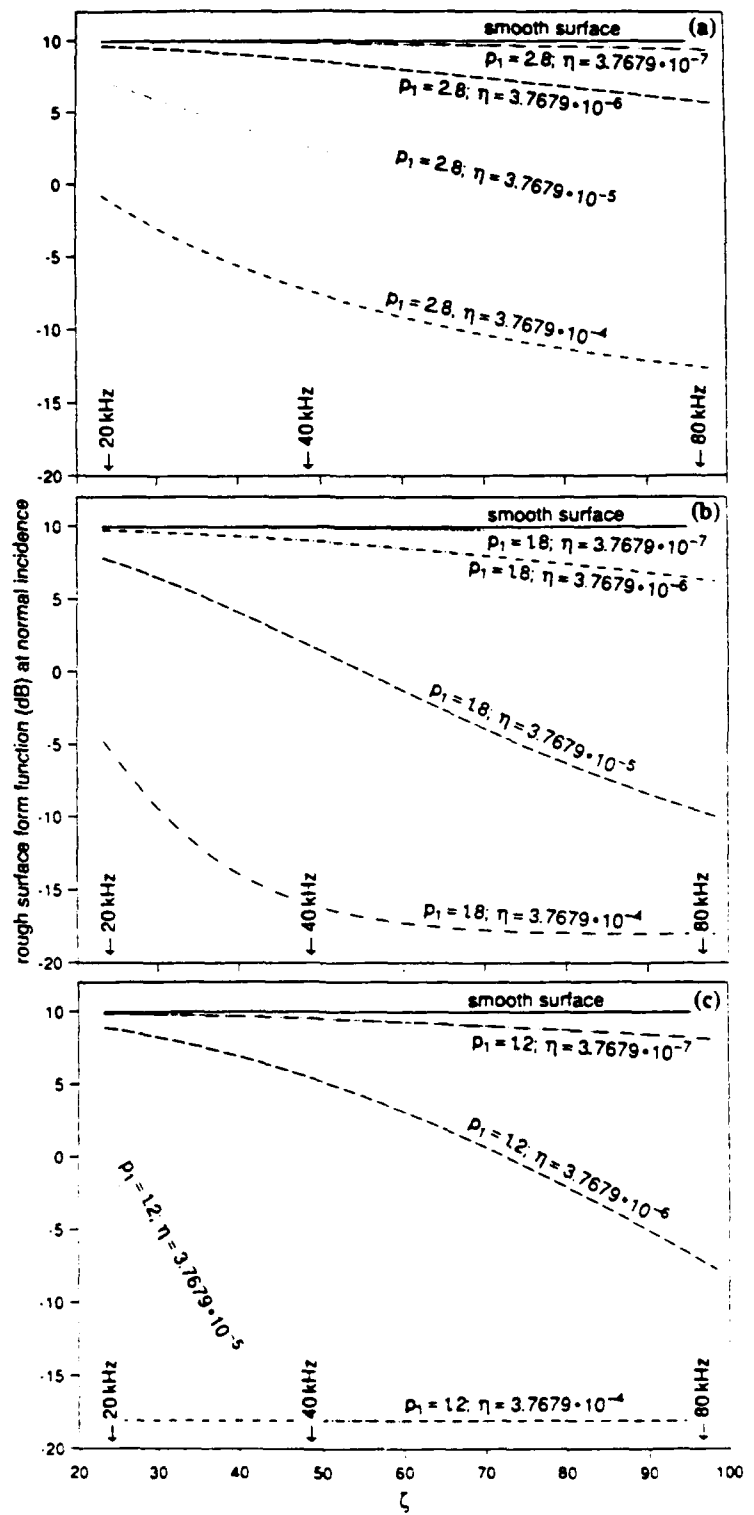
MOURAD, WILLIAMS Fig. 9



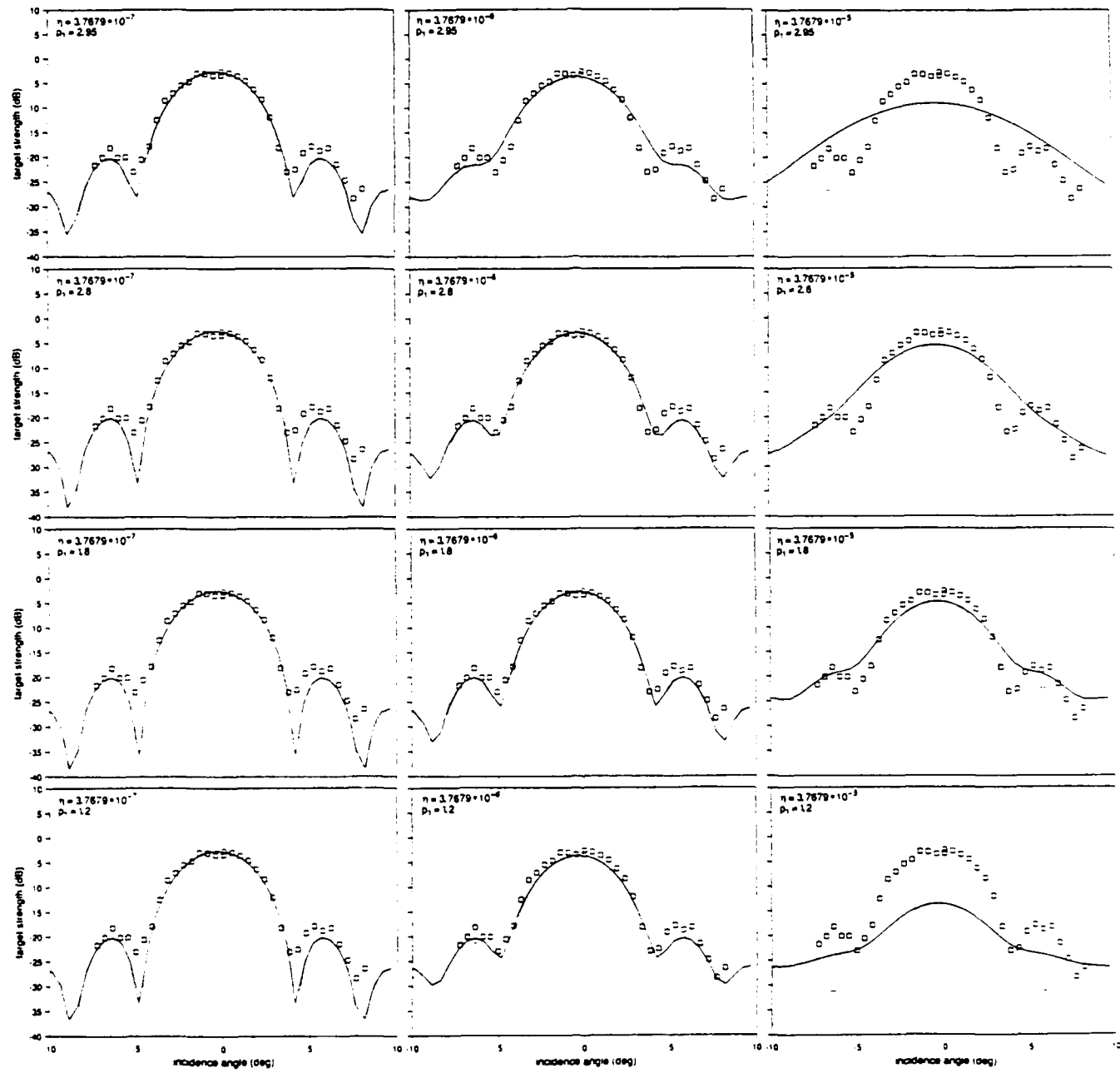
MOURAD, WILLIAMS Fig. 10



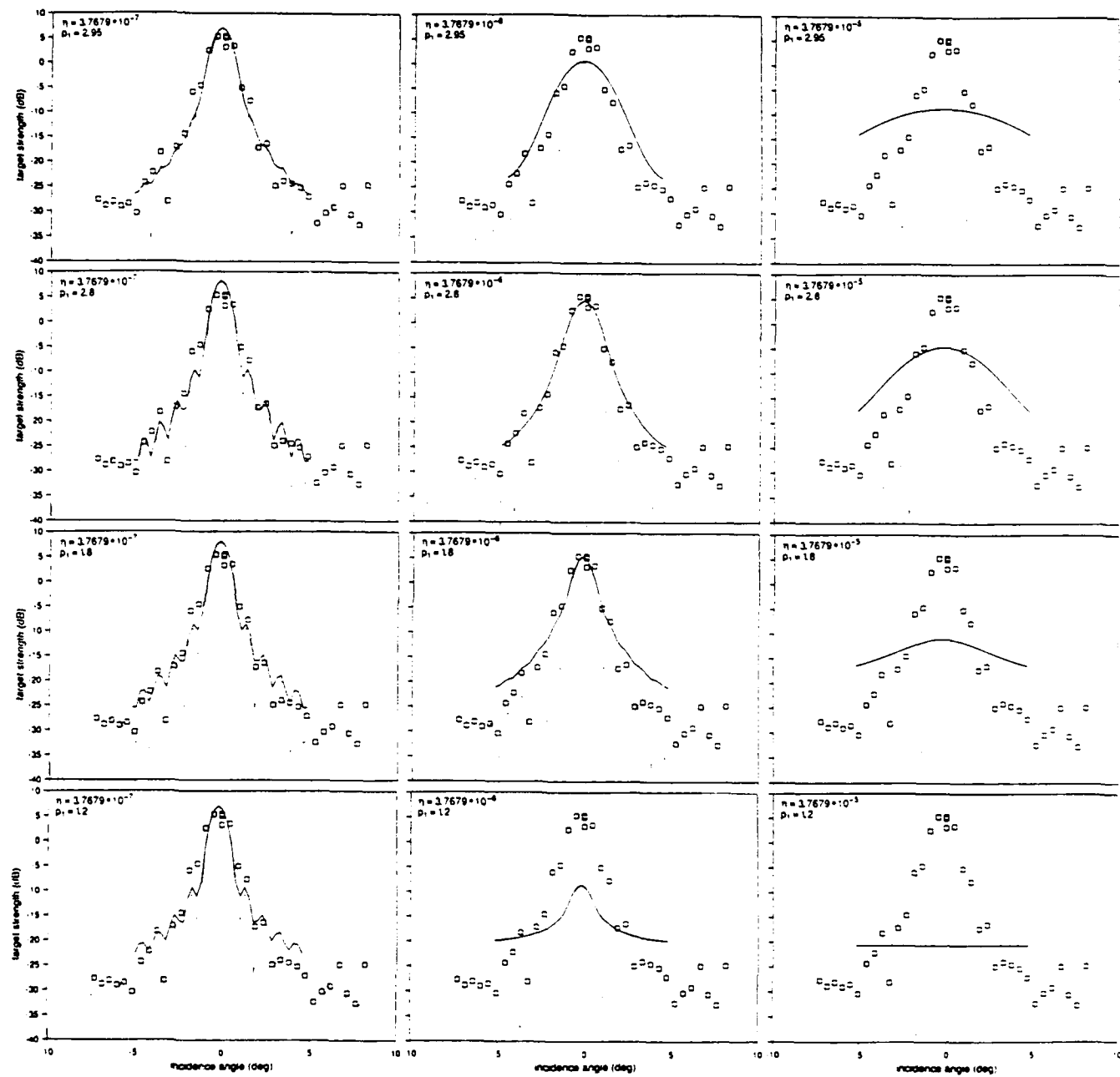
MOURAD, WILLIAMS Fig. 11



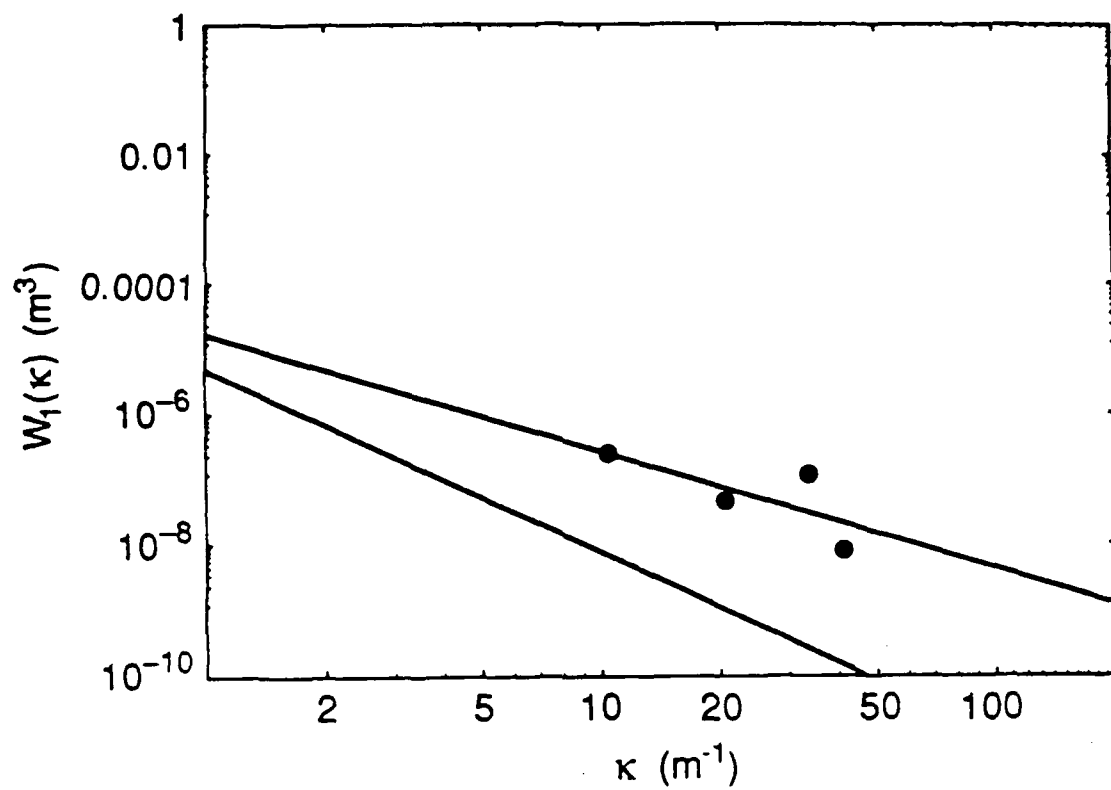
MOURAD, WILLIAMS Fig. 1



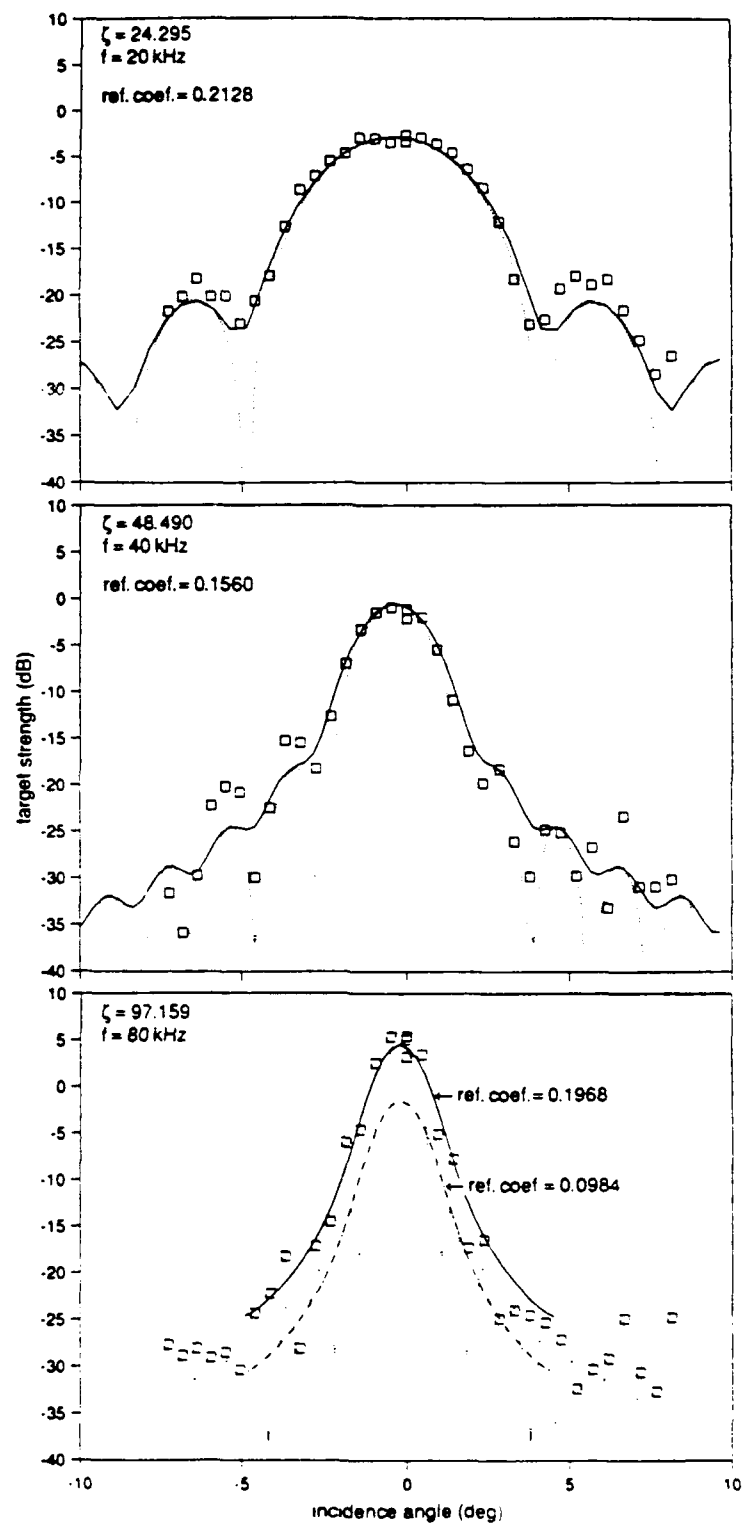
MOURAD, WILLIAMS Fig.13



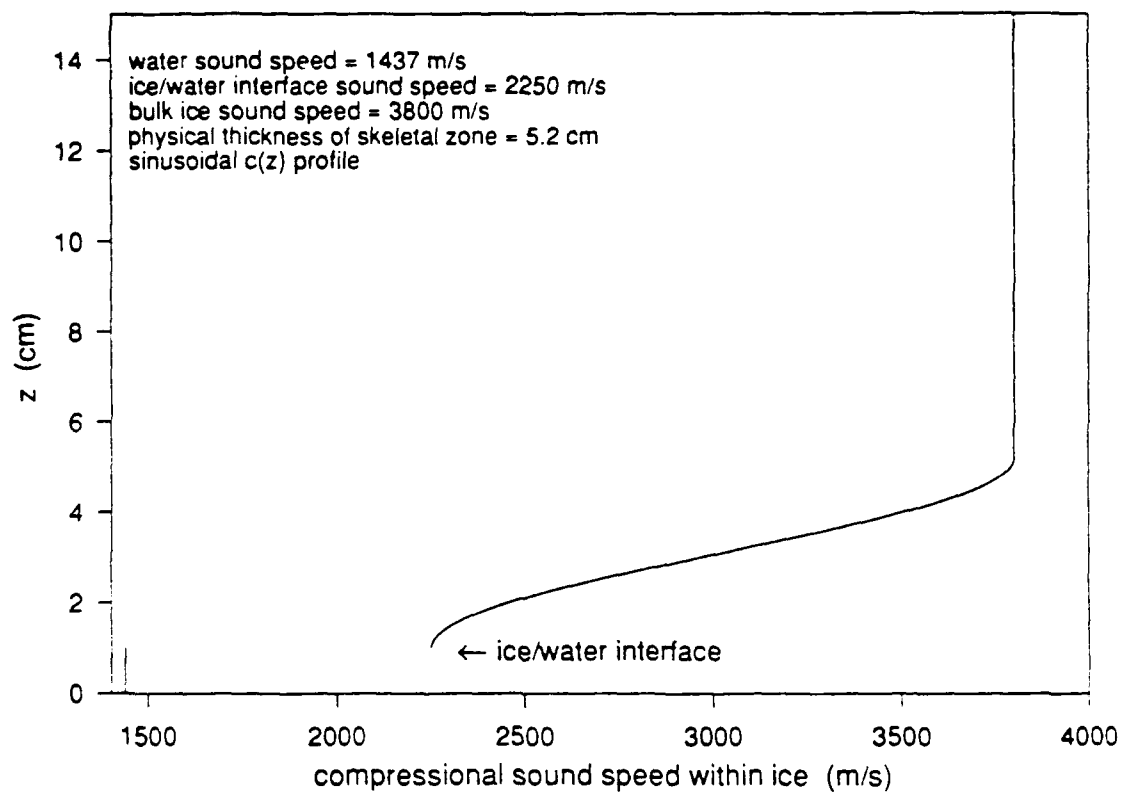
MOURAD, WILLIAMS Fig. 14



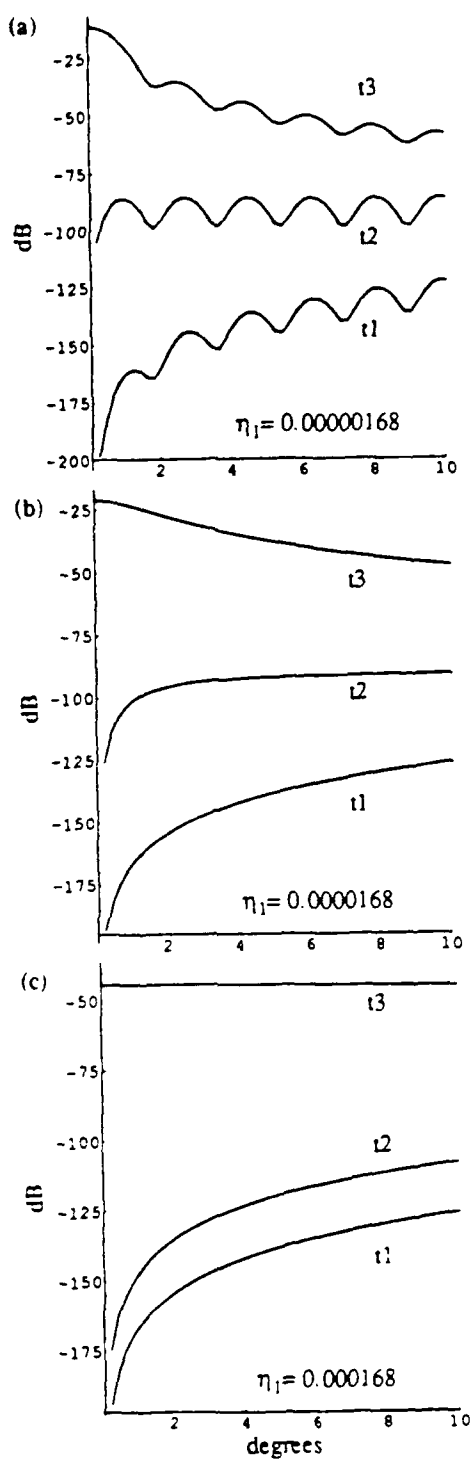
MOURAD, WILLIAMS Fig. 1:



MOURAD, WILLIAMS Fig. 16



MOURAD, WILLIAMS Fig. 17



MOURAD, WILLIAMS Fig. A

